Inclusive Cross Section of J/Psi Particles in the Far Forward Direction in $p\bar{p}$ Collisions at $\sqrt{s} = 1.8$ TeV

by

Joseph Robert Steele

A dissertation submitted in partial fulfillment of the

requirements for the degree of

DOCTOR OF PHILOSOPHY

(Physics)

at the

UNIVERSITY OF WISCONSIN - MADISON

2000

Abstract

The first measurement of the inclusive cross section of the J/ψ particle in the forward detector at CDF is presented in this thesis. Events from the Fermilab collider Run 1B and Run 1C were selected which had two forward muons that satisfied certain quality cuts, and parent J/ψs were reconstructed from the daughter muons. The efficiency and acceptance of the detector were then taken into account and the number of events turned into an inclusive cross section:

$$\sigma(J/\psi \rightarrow \mu\mu,\ \psi_{p_t} > 10\ GeV/c,\ 2.1 < |\eta| < 2.6) = 167.8 \pm 14.2\ pb \qquad (0.1)$$

Acknowledgements

As my graduate career draws to a close, my thoughts are drawn to those without whom this thesis would not have been produced. My sincere thanks go to those who struggled with me through the creation of this document.

From the FMU group, I am indebted to my advisor, Professor Lee Pondrom for his continued support. Both Lee and Professor Duncan Carlsmith evaluated my work critically and their insight has been invaluable. I am grateful to Chris Wendt for the many things he taught me, in particular, his hardware expertise is unmatched. I thank Sergei Lusin for many instructive conversations, also Jesse, George, Bob, Jim, and Hugh for their technical support. Finally, I would like to thank the hundreds of collaborators on CDF who have contributed in one way or another to the data collection and computer codes used in this analysis.

In addition to technical support, I am grateful to many of my collaborators for the knowledge and experience they have shared with me. In particular, to Jodi, Eddie, Leslie, and Carol for many instructive conversations, thank you. I learned a lot. And Eddie, for all the help with the figures in this document, thank

you.

I have had many friends during my graduate school years. For their companionship, good cheer, and fellowship, I thank Eddie, Jodi, Leslie, Lee, Mike, Carol, and, of course, Carol, Kara, Randy, Leila, Steve, Todd, Noreen, Jim, Maureen, Ken, Nancy, Brett, Paul, and Rachael.

My deepest thanks go to my parents, who have always believed in me. I would also like to thank Bruce, Mike, Todd, Al, and Debra for keeping strong family ties even over long distances.

And finally, to Ann — thank you for proofreading this thesis, and for your many helpful suggestions.

This work was supported by the United States Department of Energy Contract DE-FG02-95ER40896.

Contents

List of Tables

List of Figures

Chapter 1

Introduction

The analysis presented here is based on data taken at the Fermi National Accelerator Laboratory in Batavia, Illinois, by the Collider Detector at Fermilab (CDF). The data were taken during Run 1B and Run 1C, which were accelerator runs during 1994-95.

The Fermilab accelerator, nicknamed the Tevatron, collides protons (p) with an energy of 900 GeV, into antiprotons ($\bar{p}$) of the same energy. When relativistic (high energy) particles collide, so much energy is released that exotic forms of matter can be created.

The Collider Detector at Fermilab (CDF) is used to study particle interactions at the highest center-of-mass energy generated in any laboratory in the world. These interactions are described by the mathematical theory known as the Standard Model, and testing the predictions of this model is currently the primary

task of the CDF collaboration. To this end, this thesis measures the cross section of J/ψ production in the forward direction at CDF, using the forward muon chambers to reconstruct J/ψ particles.

The "forward" region is shorthand for both the forward and backward regions, collectively, of the detector. They are the sections of the detector that are farthest from the point of $p\bar{p}$ collision. Due to this region's proximity to the beamline, it is an area where the data have very high backgrounds. Mostly because of the high background rate, particle physics in the forward region is a largely unexplored area, therefore this measurement should constitute an important check on Standard Model predictions.

The rate at which a particular particle is created in high energy collisions is equal to the instantaneous luminosity of the experiment, times that particle's *cross section*:

$$\frac{dN}{dt} = L \cdot \sigma \tag{1.1}$$

where N is the number of a particular type of particle produced by the high energy collisions, σ is that particle's cross section, and L is the instantaneous luminosity seen by the experiment, essentially a measure of the rate of collisions. Integrating both sides of the equation over time gives:

$$N = \mathcal{L} \cdot \sigma \tag{1.2}$$

which relates the total number of particles produced to the integrated luminosity, $\mathcal{L}$, of the data set. Integrated luminosity is a measure of the size of the data set,

and is defined in Chapter 4. In this thesis, integrated luminosity will be referred to simply as luminosity, or $\mathcal{L}$, where

$$\mathcal{L} = \int L \, dt. \tag{1.3}$$

Historical aside: In the early days of particle accelerators, the physical size of nuclear components, i.e., protons and neutrons, was measured by aiming a beam of energetic particles at a target. The larger the nuclear components, the more likely they were to scatter beam particles. The equation for calculating the physical size, or component cross section, is:

$$\frac{dN_{SCAT}}{dt} = N_{BEAM} \cdot \frac{\rho \cdot N_0}{M_A} \cdot \sigma \tag{1.4}$$

where N_{SCAT} is the number of particles that are scattered by the target, N_{BEAM} is the number of particles per second in the beam striking the target, ρ is the density of the target, N_0 is Avogadro's number, M_A is the atomic weight of the target, and σ is the physical cross section of the average nuclear component. By using targets with different, known ratios of neutrons to protons, the cross section of each could be determined. In addition to simple scatterings, as particle accelerators became more energetic, these higher energy collisions began to generate new particles. The term *cross section* was retained as the name of the quantity used to measure the likelihood of a particle interaction — creation, scattering, etc.

The analysis presented here measures the cross section for the production of J/ψ particles. This is done by counting the number of J/ψ particles produced,

and dividing by the amount of data in the data set:

$$\sigma_{J/\psi} = \frac{N_{J/\psi}}{\mathcal{L}}. \tag{1.5}$$

In practice, since every detector has physical limitations, the way to determine the number of particles produced is to count the number of particles seen, and divide by the total efficiency for spotting them. Or:

$$\sigma_{J/\psi} = \frac{N_{J/\psi\ events}}{\epsilon \cdot \mathcal{L}} \tag{1.6}$$

where ϵ is the efficiency for detecting a generated J/ψ.

J/ψ particles consist of a bound state of a charm (c) and an anticharm ($\bar{c}$) quark, and hence are an example of *charmonium*. In high energy proton-antiproton ($p\bar{p}$) collisions, they are produced directly, or from decays of higher mass charmonium states (χ and $\psi(2S)$), or from bottom (b) quark decays. Six percent of J/ψ particles decay into a pair of muons [1]. Therefore, the forward muon chambers (FMU) can be used to reconstruct J/ψ particles, and calculate the cross section in the forward region. Unfortunately, since there is no way to identify forward b quarks at CDF unambiguously, it is not possible to split the measurement into the separate components from the different production mechanisms. Therefore, this calculation can only yield an inclusive cross section.

In this thesis, the second chapter provides a summary of the Standard Model, with an emphasis on the production of charmonium. Chapter 3 describes the experimental apparatus used for the analysis. Chapter 4 describes the physics

data, with emphasis on the quality cuts imposed. Chapter 5 describes the computer simulations performed to model the data, and then compares the data to the theoretical expectations that the simulations demonstrate. Chapter 6 fits the simulations to the data, calculates the J/ψ inclusive cross section, and then plots the value of the differential cross section versus transverse momentum. Finally, Chapter 7 has a summation of this analysis and comparisons to other J/ψ cross section measurements.

Chapter 2

Theory and Background

2.1 The Quark Model

Particle physics is the science which seeks to study the fundamental constituents of matter and the forces which govern their interactions. Currently, the smallest, and possibly fundamental, known subdivisions of matter are the quarks and leptons. There are six types, or flavors, of quarks and three generations of leptons, the latter each having an accompanying neutrino. The quarks are named up, down, charm, strange, top, and bottom. All six have been discovered experimentally, and experimental results indicate that there are no undiscovered quark flavors. The three types of leptons are the electron, the muon, and the tau. Partnered with them are the electron neutrino, the muon neutrino, and the tau neutrino, which bring the number of leptons to six. These particles have all

been experimentally observed as well,[1] and if there are no more than six quarks, then according to theory, there are no more than six leptons.

Quarks and leptons are among the particles called Fermions, a term which means that their spin angular momentum (a quantum mechanical quantity with no classical analog) is quantized in half integers. Particles which have integral spin, such as gravitons, photons, etc. (see section 2.2), are called Bosons.

The six quarks and six leptons can each be grouped into three generations of doublets based on the direction of their spin polarization, or helicity:

$$\begin{pmatrix} u_L \\ d_L \end{pmatrix} \quad \begin{pmatrix} c_L \\ s_L \end{pmatrix} \quad \begin{pmatrix} t_L \\ b_L \end{pmatrix}$$

$$\begin{pmatrix} \nu_{e_L} \\ e_L \end{pmatrix} \quad \begin{pmatrix} \nu_{\mu_L} \\ \mu_L \end{pmatrix} \quad \begin{pmatrix} \nu_{\tau_L} \\ \tau_L \end{pmatrix}$$

where the subscript L denotes the helicity of the particle as having left-handed polarization, i.e., its internal spin direction is in the opposite sense to that of its motion. The right-handed quarks and leptons form singlets:

$$u_R, c_R, t_R, d_R, s_R, b_R, e_R, \mu_R, \tau_R$$

There are no right-handed neutrinos or left-handed antineutrinos in the theory, and none has been observed in nature thus far.

[1]The tau neutrino has never been observed directly, but it has frequently been observed indirectly in high energy experiments.

Each one of these particles has an antimatter partner, which has the same mass, but opposite electric charge and opposite helicity. The antimatter particles are organized into the same doublets and singlets:

$$\begin{pmatrix} \bar{d}_R \\ \bar{u}_R \end{pmatrix} \quad \begin{pmatrix} \bar{s}_R \\ \bar{c}_R \end{pmatrix} \quad \begin{pmatrix} \bar{b}_R \\ \bar{t}_R \end{pmatrix}$$

$$\begin{pmatrix} \bar{e}_R \\ \bar{\nu}_{e_R} \end{pmatrix} \quad \begin{pmatrix} \bar{\mu}_R \\ \bar{\nu}_{\mu_R} \end{pmatrix} \quad \begin{pmatrix} \bar{\tau}_R \\ \bar{\nu}_{\tau_R} \end{pmatrix}$$

and

$$\bar{u}_L, \bar{c}_L, \bar{t}_L, \bar{d}_L, \bar{s}_L, \bar{b}_L, \bar{e}_L, \bar{\mu}_L, \bar{\tau}_L$$

2.2 Fundamental Forces

The four fundamental forces, or interactions, responsible for all known physical phenomena in the universe are the strong, weak, electromagnetic, and gravitational forces. In particle field theory, a force is described as being transmitted via mediating particles with integral spin, called gauge bosons.

The gauge particle for the nuclear strong force is the gluon, g. The gluon is a massless, spin = 1 particle, so named because it binds, or 'glues', the quarks together to form nucleons (protons and neutrons), and the nucleons together to form nuclei.

The nuclear weak force acts on both leptons and quarks. (The most commonly given example of the weak force is that it is the force which is responsible for nuclear beta decays.) The weak force has three massive gauge bosons, the W^+, W^-, and the neutral Z^0, each of which has spin = 1.

The electromagnetic force is quite familiar on the macroscopic level. Its mediating particle is the photon, γ, which is massless and has spin = 1.

The last of the fundamental forces, gravity, is important only on a macroscopic level, and hence is not relevant to the physics described in this thesis. It is predicted to have a spin = 2, massless mediating boson, called the graviton, but the existence of this theoretical mediating particle has not yet been experimentally verified.

2.3 Theory Development

The first component of the Standard Model was developed by Paul Dirac, when he presented his relativistic quantum theory of electromagnetism, Quantum Electrodynamics (QED) [2, 3]. It is well known that the strength of the electromagnetic force on a particle is proportional to the particle's electric charge. Dirac proposed that the force is carried by the exchange of photons between particles, a process which would be regulated by the amount of charge. While it is generally not possible to calculate exactly the strength of all possible photon exchanges between particles, a perturbation series in the QED coupling constant,

$\alpha \equiv e^2/4\pi\hbar c \approx 1/137$, converges rapidly. When using perturbation theory to calculate the matrix element that describes an electromagnetic process, each photon that is emitted or absorbed contributes one power of α to the square of the matrix element, and hence to the probability of the exchange. So processes requiring a larger number of photons are suppressed relative to those with fewer photons. This makes it possible to calculate very good approximations to the strength of the electromagnetic force by looking at only "lower-order" processes, in which only a few photons are exchanged.

QED has been extended by Glashow, Weinberg, and Salam [4, 5, 6] to include the weak force. One difference between electromagnetism and the weak force is that all three weak gauge bosons are massive, which has the effect of limiting the range of the force when the energy transfer is smaller than the $W^{\pm}$ or Z^0 mass. However, if the energy transfer is larger than those masses, the weak force behaves similarly to the electromagnetic force. In this high energy realm, the two forces are said to *unify* into a single force, the *electroweak force*, with a single coupling constant related to α.

The final force incorporated at the quantum level in the Standard Model is the strong force, which binds quarks into *hadrons*: either *baryons* or *mesons*. A baryon consists of three quarks, while a meson is the bound state of a quark and an antiquark. The strong force is mediated by eight gluons, whose coupling is proportional to the charge of the strong force, or *color charge*. The properties of gluons are described by the theory of Quantum Chromodynamics (QCD). QCD

and the electroweak force are not yet unified within the context of the Standard Model, so there is a second coupling constant, α_s, which is unrelated to α, and which describes the strength of the QCD force. Because α_s is substantially larger than α, the QCD force is called the strong force, and α_s the *strong coupling constant.*

2.4 Charm Quark Discovery

One early objection to electroweak theory was that it predicted events where the quark flavor would be changed without a change of electric charge (i.e., a neutral current). Specifically, with the three quarks that were known before 1974, it was predicted that energetic d quarks (electric charge = $-1/3$ electron charge) could change into s quarks (electric charge = $-1/3$ electron charge, also), and s quarks could decay into d quarks. However, these *flavor-changing neutral currents* were not seen experimentally.

This prediction comes about because the electroweak quark eigenstates are linear combinations of the QCD quark eigenstates, so the amplitude for a process such as $\nu_\ell d \to \nu_\ell d$ scattering is actually the weighted sum of the amplitudes for the processes $\nu_\ell d' \to \nu_\ell d'$ and $\nu_\ell s' \to \nu_\ell s'$ shown in Figure 2.1, where

$$d' = d\cos\theta_C + s\sin\theta_C \tag{2.1}$$

$$s' = s\cos\theta_C - d\sin\theta_C \tag{2.2}$$

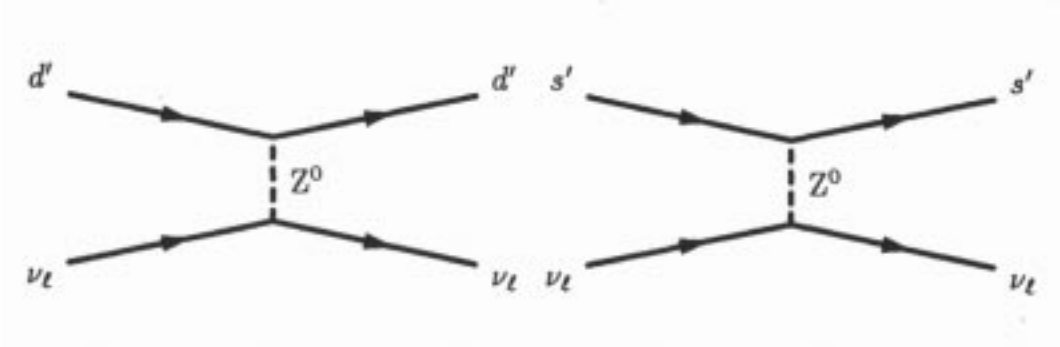

Figure 2.1: Predicted flavor changing neutral current events. Since the d' and s' are mixtures of d and s quarks, both diagrams include d and s quarks in both the initial and final states.

where the *Cabibbo angle*, θ_C, is a theory parameter which must be measured experimentally.

At the time electroweak theory was first proposed, there were only three known quarks: u, d and s. The u and d quarks formed an isospin doublet (actually, (u, d')), but the s quark could only be put into a singlet (s'). The prediction comes about because the Z^0 couples with different strengths to singlets and doublets, so the $d \rightarrow s$ components do not cancel completely, leaving some interactions where d's become s's, and some where s's become d's. Thus, the theory predicts interactions where quark flavor is changed, but no charge is exchanged, with a cross section similar to that of $\nu_\ell d \rightarrow \nu_\ell d$. Experimentally, flavor-changing neutral currents are nearly absent [7] — a serious problem for the theory.

In 1970, Glashow, Iliopoulos, and Maiani [8] demonstrated that this problem could be resolved by the addition of a fourth quark to the picture. The s quark and the proposed fourth quark would form an isospin doublet, and the couplings in the two diagrams would then be equal. The $d \rightarrow s$ transitions would cancel, and the flavor-changing neutral currents would no longer be allowed by the theory. Thus, the proposed fourth quark becomes the "charm" that eliminates the unwanted prediction, yielding the quark's name. However, at that time, there was no experimental evidence for the charm quark.

This changed with the "November Revolution" in 1974. Working separately, experiments using a proton beam on a beryllium target at Brookhaven [9], and an electron-positron collider at SLAC [10], both found evidence of a narrow resonance with a mass of about 3.1 GeV/c^2. The results of the Brookhaven experiment are shown in Figure 2.2.

If this resonance were an excited state formed from a combination of up, down, and strange quarks, it should decay via the strong force, with a much larger width (i.e., a much shorter half-life). The narrow width (, $_{\psi} = 87 \pm 5$ keV [1]) made it clear that a new type of quark was involved.

The particle was named the J by the Brookhaven group, and the ψ by the SLAC group. To note the unique simultaneous discovery, the particle is now called the J/ψ.

By scanning the cross section near the J/ψ mass, the SLAC group was able to observe $J/\psi - \gamma$ interference. This, combined with the fact that it is produced

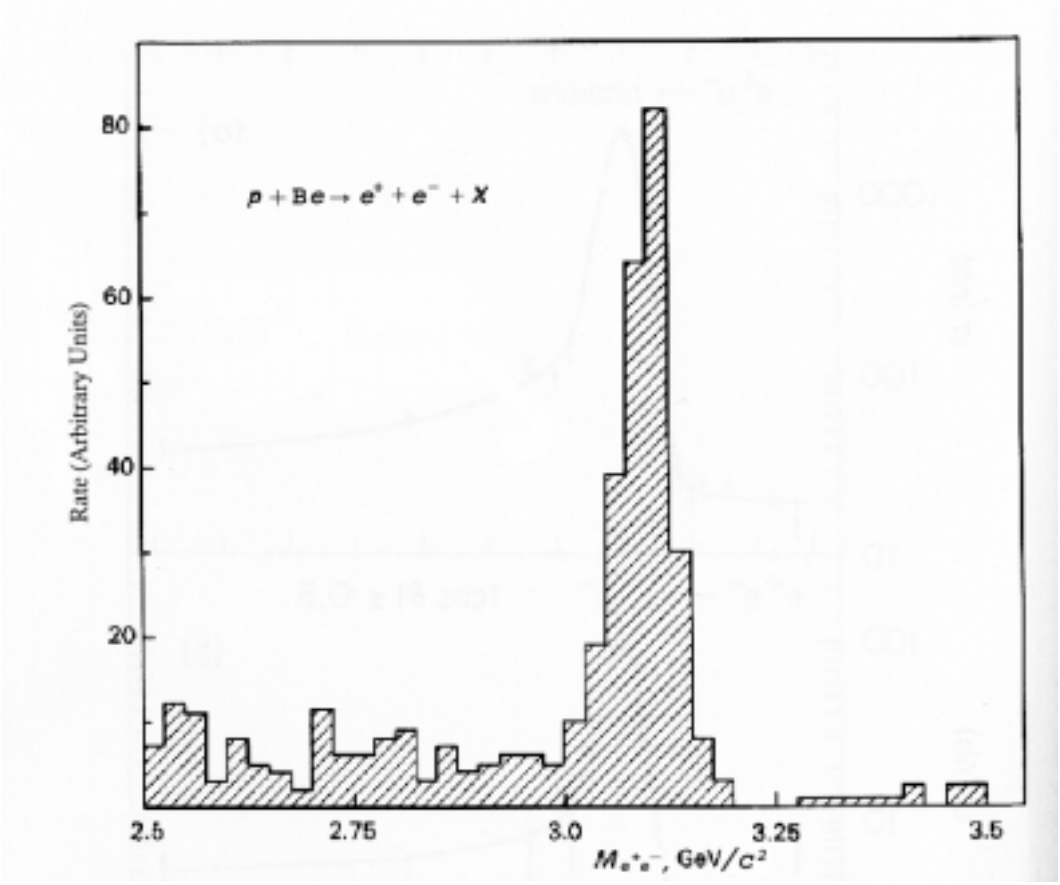

Figure 2.2: Results of the Brookhaven National Lab 1974 experiment. This plot shows the narrow resonance of the J/ψ in the invariant mass distribution of e^+e^- pairs produced in collisions of protons with a beryllium target (p + Be$\rightarrow$ $e^+ + e^- + X$).

directly in e^+e^- collisions, leads to the conclusion that the J/ψ has the same quantum numbers as the photon. Shortly thereafter, the SLAC group reported a second resonance at 3.7 GeV/c^2 [11] . Now called the ψ' or $\psi(2S)$, this was later determined to be a radial excitation of the first resonance. These states and other $c\bar{c}$ bound states are collectively referred to by the generic name charmonium.

2.5 Charmonium Production

Two processes dominate the production of charmonium in $p\bar{p}$ collisions. The first of these is known as direct, or prompt, production. It's the production of a $c\bar{c}$ pair directly from the initial particle collision, where the two quarks combine to produce a colorless bound state, as in Figure 2.3. The other process is the production of a b or $\bar{b}$ quark in the initial collision, which then forms a B hadron (a hadron — anything made up of quarks — with at least one bottom quark in it). This hadron can subsequently decay into a ψ and other hadrons, as in Figure 2.4.

2.5.1 Direct Production

The leading order Feynman diagrams for direct ψ and χ_c production in $p\bar{p}$ collisions are shown in Figure 2.3. The $c\bar{c}$ quarks are produced in a color-singlet state, and the entire diagram can be calculated, except for the "blob" representing the hadronization of the quarks into a ψ or χ_c meson. The ψ diagram can

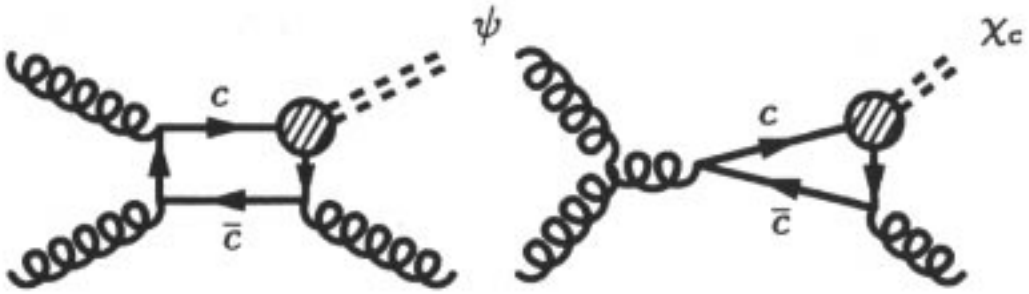

Figure 2.3: Feynman diagrams for charmonium production. On the left is the leading order diagram for direct J/ψ and $\psi(2S)$ production. On the right is the leading order diagram for direct χ_C production.

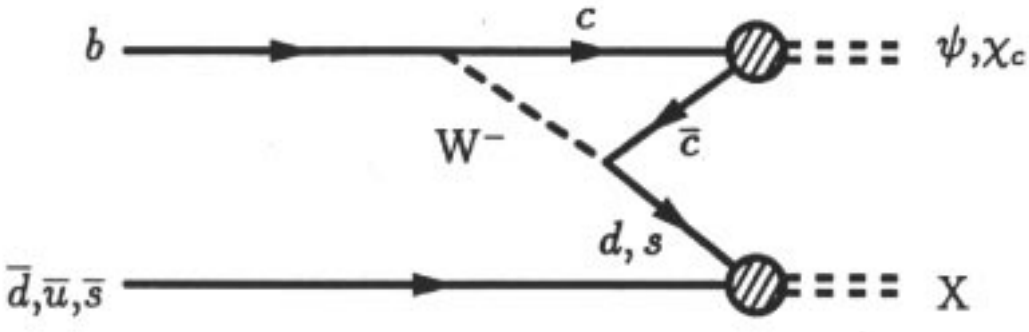

Figure 2.4: Typical B meson decay diagram for charmonium production.

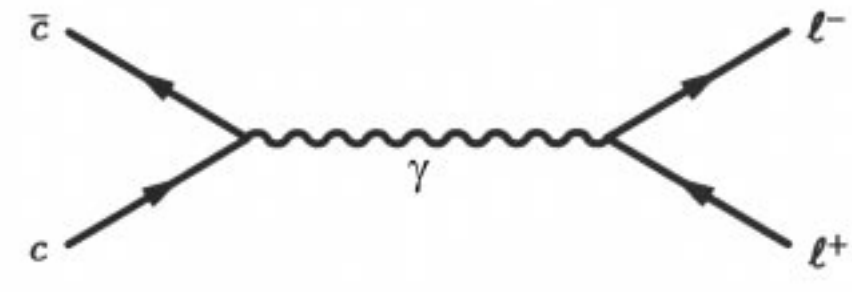

Figure 2.5: Feynman diagram for the decay $\psi \to \ell^+\ell^-$

be calculated up to a factor related to the amplitude of the ψ wave function at the origin, $|\psi(0)|^2$, and the wave function itself can be determined from the ψ leptonic decay width.

The decay $\psi \to \ell^+\ell^-$ is shown in Figure 2.5. The partial width for this decay can be derived from the figure, and it is given by [12, 13]:

$$, _{\ell^+\ell^-} = \frac{16\pi\alpha^2 Q^2}{M_\psi^2}|\psi(0)|^2 \tag{2.3}$$

where $\ell = e, \mu, \tau$ and $Q = \frac{2}{3}$ is the charm quark charge, and M_ψ is the mass of the ψ. The photon propagator contributes a factor of $1/q^2 = 1/M_\psi^2$ (where q is the momentum carried by the photon). The $c\bar{c}\gamma$ vertex contributes a factor of $Q\sqrt{4\pi\alpha}$ and the $\ell^+\ell^-\gamma$ vertex contributes a factor of $\sqrt{4\pi\alpha}$, yielding

$$|\mathcal{M}| \propto \frac{4\pi\alpha Q}{M_\psi^2}. \tag{2.4}$$

or

$$|\mathcal{M}|^2 \propto \frac{\alpha^2 Q^2}{M_\psi^4}. \tag{2.5}$$

The matrix element for the $c\bar{c}$ annihilation is proportional to $q^2|\psi(0)|^2$, leaving the $1/M_\psi^2$ dependence. Except for the wave function, all of the quantities on the right hand side of equation 2.3 are known. Thus, a measurement of , $_{\ell^+\ell^-}$ yields a measurement of the ψ wave function at the origin.

There is a similar production mechanism which only contributes to J/ψ production. The $c\bar{c}$ pair can form a χ_c state, which decays to a J/ψ through an electromagnetic transition ($\chi_c \rightarrow J/\psi + \gamma$). As all the known χ_c states are below the $\psi(2S)$ mass, this mechanism does not contribute to $\psi(2S)$ production.

As seen in Figure 2.3, ψ production diagrams contain charm quark loops which are connected to three gluons, while the charm quark loops in the χ_c production diagrams are connected to only two. This is a result of G-parity conservation.[2] Since the gluon has negative G-parity, a state consisting of N gluons has $G = (-1)^N$. Thus, the ψ, with odd G-parity, only couples to states with an odd number of gluons, while the χ_c, with even G-parity, can only couple to states with an even number of gluons.

2.5.2 B Production

The other mechanism for ψ production is the decay of B hadrons. The initial collision produces a b quark, which forms a B hadron that subsequently decays

[2]G-parity is a conserved quantity for strong interactions. It is simply an isospin rotation, followed by charge conjugation.

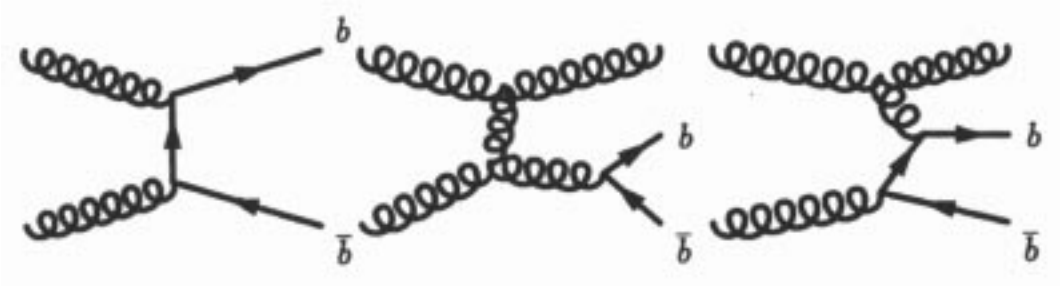

Figure 2.6: Feynman diagrams for b production from gluon fusion (left), gluon splitting (center), and flavor excitation (right).

into a ψ and other particles. At next-to-leading order, the diagrams for b quark production can be grouped into three classes, shown in Figure 2.6. Each of these processes has distinct characteristics. The first diagram depicts an example of incident gluons colliding to produce a b quark pair. The two b quarks produced by this gluon fusion are separated by π radians in azimuthal angle, and typically produce two well separated jets.

The second diagram shows an example of gluon splitting. Gluon splitting tends to produce b quarks which are closer together, due to the fact that the mass of the virtual gluon tends to be small. As a result, the decay products of the two quarks may appear to come from a single parent, especially after fragmentation effects and experimental resolution are included.

Finally, flavor excitation, shown in the third diagram, is often the result of the gluon scattering off one of the virtual b quarks, which form a cloud around the valence quarks. When this occurs, the second b proceeds close to the initial proton

or antiproton direction. This process is expected to contribute significantly to J/ψ events in the forward/backward region.

After the b quark forms a B hadron, it can decay to a ψ or χ_c meson through diagrams such as those in Figure 2.4. This decay channel is suppressed relative to the decay $B \rightarrow D + X$, for several reasons. First, the W boson in Figure 2.4 must decay into $\bar{c}s$, however, in the $B \rightarrow D + X$ decay, all of the possible W decay modes are allowed. This reduces the relative rate by about a factor of three. Furthermore, the $\bar{c}$ and the c quark must be opposite in color, since QCD requires a bound state to be color neutral. This reduces the rate by another factor of three. Lastly, the c and $\bar{c}$ quarks must have similar momenta, in order for it to be kinematically possible to form a bound state. This results in decays with the relatively small branching ratios of $\mathcal{B}(B \rightarrow J/\psi \ + \ X) = 1.13 \ \pm \ 0.06$ % [1] and $\mathcal{B}(B \rightarrow \psi(2S) \ + \ X) = 0.35 \ \pm \ 0.05$ % [1].

The J/ψ subsequently decays into two muons with a branching ratio of $\mathcal{B}(J/\psi \rightarrow \mu \ \mu) = 6.01 \ \pm \ 0.19$ % [1]. While these branching ratios are small, it is an experimental fact that the two muons from the ψ decay provide a clean signature to use to identify and analyze events, so the process $B \rightarrow \psi + X$ is tremendously useful to experimentalists.

2.6 Masses and Decay Modes

Naively, one would expect that charmonium would decay quickly, as the $c\bar{c}$ pair would annihilate into gluons, producing a broad resonance. While this does happen, it occurs at a lower rate than in other strong decays, due to several factors. After the $c\bar{c}$ pair annihilates into gluons, one or more of the resulting gluons must carry away most of the energy, about 3 GeV. This is a high enough energy that α_s is fairly small, which reduces the rate for the process. Also, color conservation requires that at least two gluons be emitted. In the discussion of ψ production, we saw that G-parity prohibits the production of a ψ from two gluons, thereby requiring three gluons. The same is true for the decay of a ψ — again, three gluons are required. As a result, the decay is a higher order process than are most other strong decays, since most strong decays exchange only one soft gluon. Finally, three body phase-space is highly suppressed relative to two body phase-space, i.e., the kinematics involved discourage three body decays.

The combination of all of these factors suppresses the rate at which this strong force decay takes place. Electromagnetic decays, in which either the pair annihilates into a virtual photon, or a real photon is emitted, form a significant fraction of the decays of many charmonium states.[3]

---

[3]One exception is states with masses larger than twice the D mass (see Chapter 5 for a description of the D). These decay almost exclusively into $D\bar{D}$. Since such decays proceed by the exchange of one soft gluon, the rate for these decays is much higher than the rate of

The internal dynamics of the charmonium system are similar to those of the hydrogen atom or the positronium system. One difference is that, while positronium is bound together by exchanges of soft photons, charmonium is bound by exchanges of soft gluons. Therefore, while accurate calculations are possible for the energy levels of positronium, similar calculations for the masses of charmonium states are much more difficult. However, the quantum numbers that are used to describe positronium can also be applied to charmonium. The rotational quantum number in positronium results from the rotational invariance of the potential, while the radial quantum number is the number of nodes of the radial wave function plus 1. The QCD quark-quark potential has similar properties, so similar quantum numbers exist, although the dependence of the energy levels is different.[4]

The lightest charmonium state is the η_c. In an η_c, the $c\bar{c}$ pair is in an S-wave state[5], with the quark spins anti-parallel. The next higher state is the J/ψ, which

---

radiative decays to other charmonium states.

[4]Just as in positronium, the spin–orbit coupling breaks the rotational symmetry. While the effect is larger than it is in positronium, it can still be treated as a small perturbation.

[5]S, P and D waves refer to the spatial portion of the wave function. (e.g., an S wave state has $L = 0$ and $J = 0$ or 1, depending on the configuration of the spins.) The spectroscopic notation generally used in nuclear and particle physics uses the radial quantum number, not the principal quantum number as in atomic physics. One difference from atomic spectroscopic notation is that, for orbitally excited states, the radial quantum numbers start from 1 for each

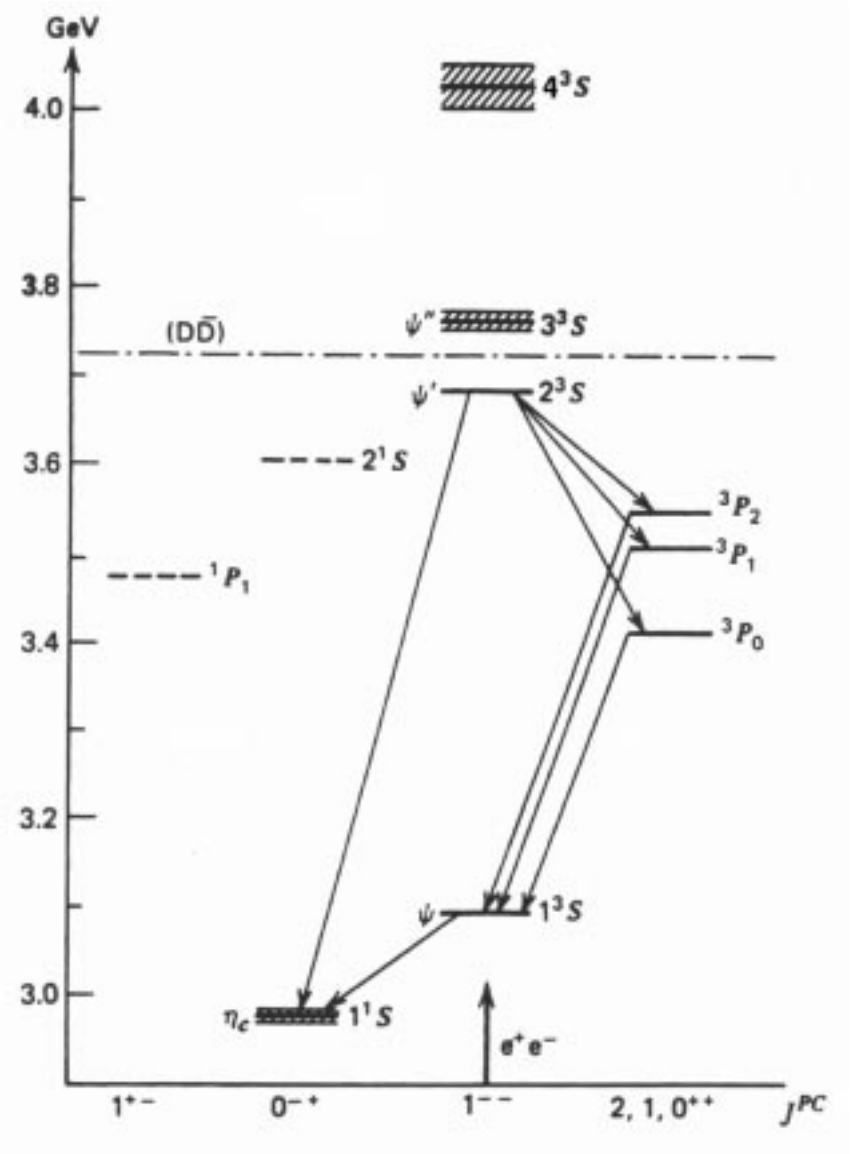

Figure 2.7: Charmonium mass spectrum. States with masses above the $D\bar{D}$ threshold (the dot-dash line) decay almost exclusively into charmed (D) mesons. The particle widths are shown by shaded bands. (Taken from Fig. 2.13 in *Quarks and Leptons*, F. Halzen and A. D. Martin, 1984.)

is the S-wave state with parallel spins. The excited S-wave states are sometimes denoted by $\psi(n\mathrm{S})$ or by ψ', ψ'', etc. The P-wave states with parallel spins are denoted as χ_{c_J}, where $J = 0, 1, 2$ is the total angular momentum of the state. χ_c is a generic term that refers to any of the χ_{c_J}. Figure 2.7 shows the charmonium mass spectra and decay modes to other charmonium states. Other states, such as the P-wave spin singlet, and D-wave states, are expected to exist, but are not expected to contribute significantly to ψ production.[6]

2.7 ψ Production in the Forward Direction

In the 1990's, CDF measured a surprising excess of J/ψ and $\psi(2S)$ mesons in the detector's central region [14]. This excess was approximately a factor of 50 in the prompt production of $\psi(2S)$ mesons. This measurement caused high energy physics phenomenologists to re-evaluate their models of ψ production. The result of this re-evaluation is that the formerly popular Color Singlet Model fell out of favor, and the Color Octet Model has become the leading theory of ψ production [15, 16].

---

value of L. Thus, while the lowest lying $L = 1$ states are typically denoted by $2^S\mathrm{P}_J$ by atomic physicists, the particle physics designation is $1^S\mathrm{P}_J$.

[6] Feeddown from the P-wave singlet is suppressed, because of the need to flip the spin of one of the quarks, and the decay of a D-wave state to a ψ requires $\Delta L = 2$, which is suppressed by an additional power of α.

When particles are produced from a high energy collision, they travel away from the initial collision at angles which depend, in part, on the energy of the collision. A convenient unit for one of these angles is called *rapidity*. Rapidity, y, is defined as

$$y \equiv \frac{1}{2}\ln(\frac{E + P_Z}{E - P_Z}) \tag{2.6}$$

where E is the energy of the produced particle, and P_Z is the fraction of the particle's momentum that is longitudinal (parallel) to the direction of the incident particles that cause the initial collision. Rapidity is a convenient unit to measure the outgoing angle, where $y = 0$ is completely perpendicular to the incident particles, and large values of y, positive or negative, are along the directions of the incident particles.

The precise angular dependence of prompt J/ψ production is determined by the theoretical model used to calculate it. Thus, measurements of J/ψ production at different rapidities would provide useful checks on the various theoretical models.

In 1996, HEP phenomenologist Sean Fleming used the Color Octet Model to calculate the cross section for direct J/ψ production in the forward region. His calculations revealed that the direct production of J/ψ particles decreases with increasing rapidity [17]. Fleming's plot is reproduced in Figure 2.8. From the bottom curve, which plots direct production of J/ψs with a $\psi_{p_t} = 11$ GeV/c (ψ_{p_t} is the transverse momentum of the ψ, or the component of the momentum that is perpendicular to the particle beam), the differential cross section at the center

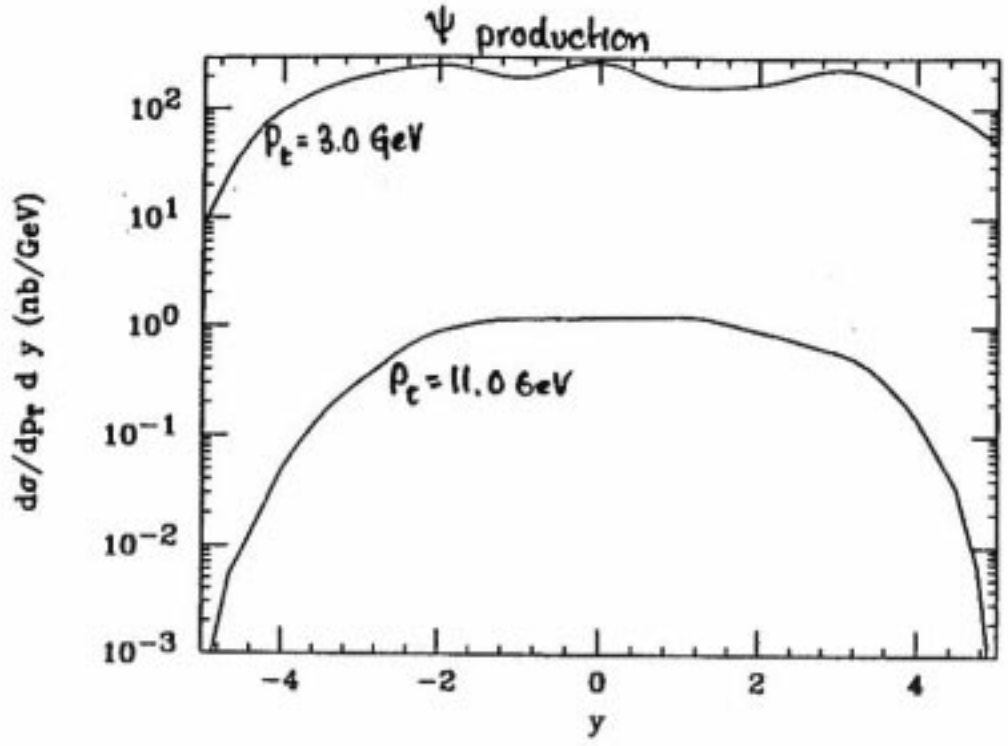

Figure 2.8: The cross section for prompt ψ production, versus rapidity.

of the detector ($y = 0$) is about 1.2 nb/GeV/c (nanobarns per GeV/c). However, at $y = 2.3$, the average rapidity of the analysis in this thesis, the differential cross section falls to 0.8 nb/GeV/c, a one third decrease.

This calculation has never been checked experimentally, but if it is accurate, it shows that we should expect the forward direct J/ψ signal to be suppressed relative to central events. This would result in a smaller inclusive cross section in the forward region.

2.8 B Production in the Forward Direction

The analysis presented in this thesis requires particles to have a transverse momentum above a certain minimum. Combined with the angle a particle has to take from the initial collision to reach the forward region, this requires that forward particles have a relatively large momentum.

HEP phenomenologists have recognized that there are higher-order corrections to the calculation of the b quark production cross section, which are potentially large, which depend on the transverse momentum of the b. In fact, at large momentum, the b quark behaves more and more like a massless particle, radiating an increasingly large amount of its energy in the form of hard, collinear gluons. These momentum dependent corrections could easily result in different cross sections in the central and in the forward regions. Naturally, different b quark cross sections would result in different cross sections for J/ψ particles produced from b quarks decays.

There have been attempts to compute the cross section for bottom quark production in the forward region. In 1998, Frixione, Mangano, Nason, and Ridolfi calculated the inclusive muon distribution from the decay of b quarks versus rapidity, and compared it to experimental data [18]. These experimental data were recorded by D0, which is the other colliding physics experiment at Fermilab.

The differential cross section in muon variables is not the same as the differential cross section in bottom quark variables, but monte carlo simulations

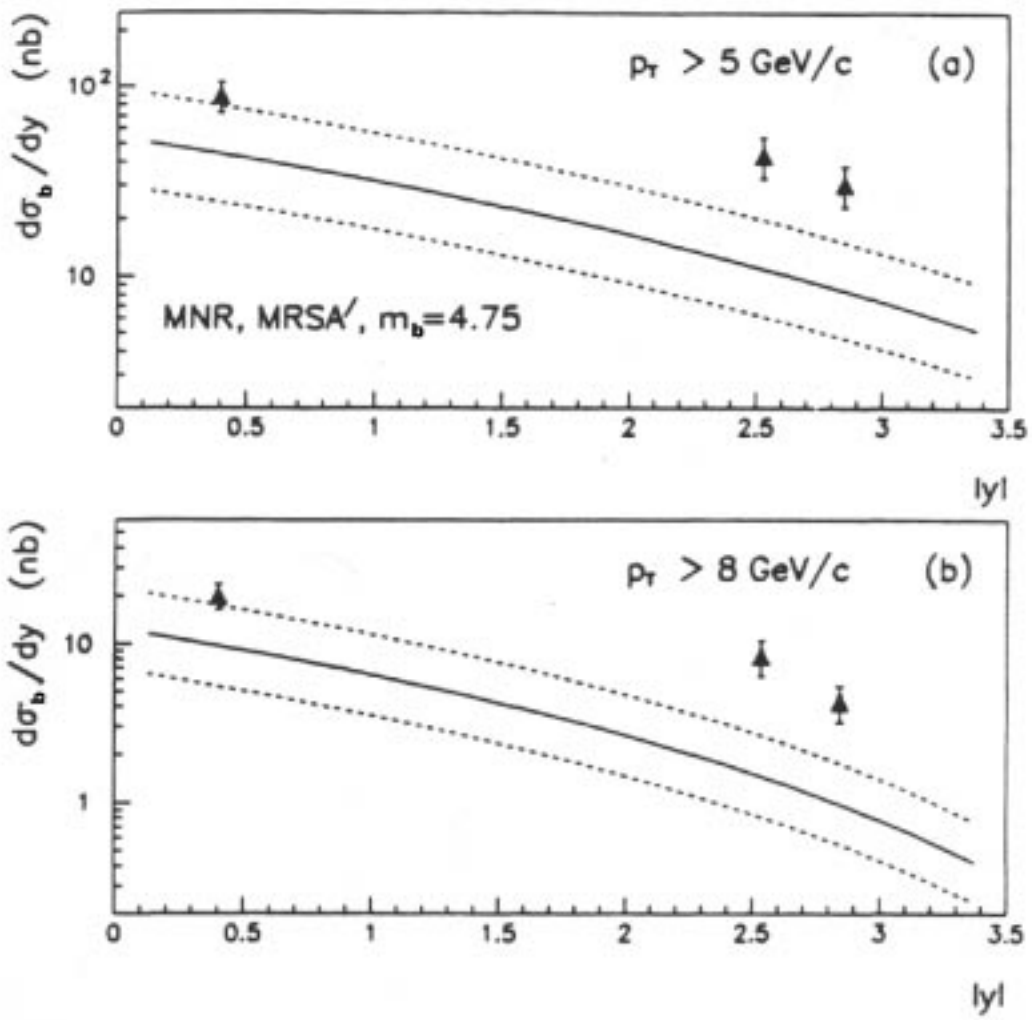

Figure 2.9: Comparison between D0 data (triangles) and theory (curves) for the $p\bar{p} \rightarrow (b \rightarrow \mu) + X$ cross section, versus muon rapidity. (a) Muon has transverse momentum greater than 5 GeV/c. (b) Muon has transverse momentum greater than 8 GeV/c.

show that these two cross sections are well correlated [19]. Because of this, any change versus rapidity of the b cross section with a required muon would indicate a change versus rapidity of the total b cross section.

The results of this comparison are shown in Figure 2.9. The data points are the experimental data recorded by D0, and the curves are the calculated cross sections. The solid line shows the central value of the theoretical calculation, while the dotted lines show the theoretical uncertainty. This uncertainty was calculated by varying two parameters: the mass of the b quark, which was varied from 4.5 $GeV/c^2 < m_b < 5$ GeV/c^2, and the renormalization scale, μ, which was varied from $\mu_0/2 < \mu < 2\mu_0$. μ_0 is a reference scale chosen in this calculation to be $\mu_0 = \sqrt{m_b^2 + p_t^2}$, i.e., the b quark mass and its transverse momentum, added in quadrature. Figure 2.9 (a) displays the calculated cross section when the muon produced from the b quark decay has transverse momentum greater than 5 GeV/c, and Figure 2.9 (b) displays the same calculation when the muon p_t is greater than 8 GeV/c.

These plots display the $p\bar{p} \rightarrow (b \rightarrow \mu)$ cross section versus the absolute value of detector rapidity. The horizontal axis is labeled $|y|$, to indicate that the results apply to either the forward region (positive rapidity) or the backward region (negative rapidity). Both of these plots show a definite fall-off in the theoretical calculation. The higher energy plot is more relevant to the analysis presented here, and the $p_t > 8$ GeV/c plot shows the sharper decrease. However, the D0 data don't confirm a fall-off as steep as calculated. (This discrepancy, again,

provides impetus for more forward measurements.)

The D0 data in Figure 2.9 (b) show a $p\bar{p} \rightarrow (b \rightarrow \mu)$ cross section of 20 nb (nanobarns) at a rapidity of 0.4, which is inside the central region. This cross section becomes about 8 nb at a rapidity of 2.5, a value within the forward/backward region, and close to $y = 2.3$, the average rapidity of the analysis presented in this thesis. This 60% decrease is even steeper than the predicted decrease in prompt production (as seen in the previous section). The central theory curve changes from a cross section of 10 nb at $y = 0.4$ to about 2 nb at $y = 2.5$. However, this 80% decrease is steeper than the data confirm. These results lead us to expect the number of forward $B \rightarrow J/\psi$ events to be suppressed relative to the number of events in the central region.

2.9 Fraction of J/ψ Events from B Decays

In the central region, CDF measured the fraction of all J/ψ events that come from B hadron decays [14]. Figure 2.10 plots this fraction, f_B, versus the transverse momentum of the ψ particle. The upper curve (triangles) plots f_B for ψ' events, and the lower curve (circles) shows f_B for J/ψ events.

The graph shows a clear p_t dependence. For a $\psi_{p_t} > 10$ GeV/c (the minimum p_t for the analysis in this thesis), approximately 25% of the J/ψ events are the result of B hadron decays, leaving prompt production to account for the other 75%. This value ($f_B = 0.25$) rises to about 40% for higher values of the J/ψ

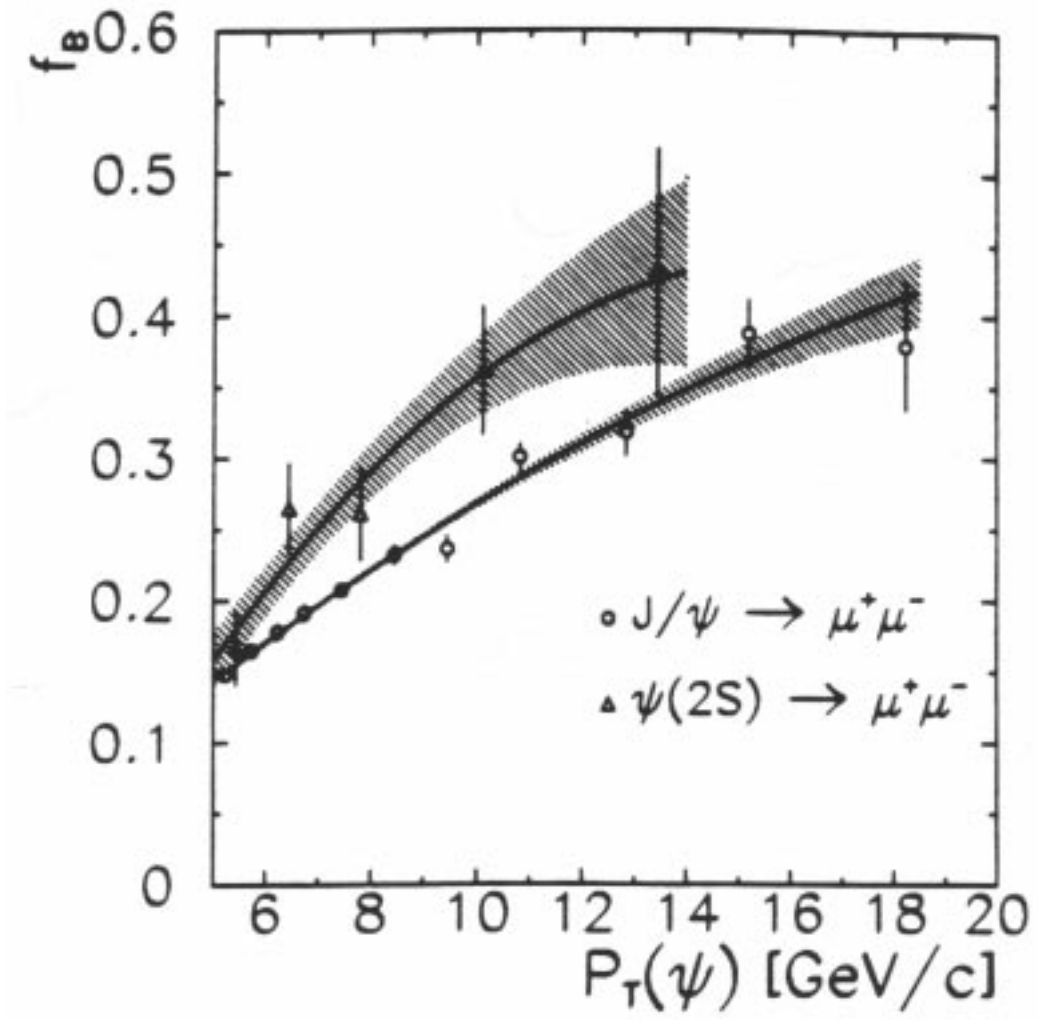

Figure 2.10: The fractions (f_B) of J/ψ (circles) and $\psi(2S)$ (triangles) originating from B hadron decays. The error bars indicate the combined statistical and systematic uncertainties on the fractions. The solid curve is the fitted function, and the slashed regions indicate the uncertainty in the fit.

transverse momentum.[7] Therefore, the central data show that, in this momentum range, the ratio of J/ψs that come from B decays to prompt J/ψs, is between 1/3 and 2/3.

In the forward region at CDF, it's not possible to tag b quarks the same way they're tagged in the central region.[8] Because of this, the fraction f_B can not be measured there. However, calculations backed by experimental data show that the cross section for b quark events is expected to decrease in the forward region (Section 2.8), and calculations without experimental confirmation show that the cross section for J/ψ prompt production is also expected to decrease (Section 2.7). Therefore, the central values of f_B might hold in the forward region as well.

---

[7] f_B for $\psi(2S)$ events is slightly higher, but because so few $\psi(2S)$ events are expected, compared to the number of J/ψ events, we can safely ignore that small excess.

[8] In the central region, the Silicon Vertex Detector (SVX) is used to identify a secondary vertex, i.e., a b decay vertex, which indicates a b quark event.

Chapter 3

Experimental Apparatus

The Collider Detector at Fermilab (CDF) is designed to measure the momentum and energy of electrons, photons, muons, hadrons and jets. The forward muon (FMU) detector is one component of the CDF detector. In this chapter, I will describe the experimental facilities at Fermilab, and the detector components used in the identification and momentum measurement of forward muons.

3.1 The Tevatron Collider

The accelerator at Fermilab consists of several stages of particle acceleration to reach the final collision energy of 900 GeV in each beam. Figure 3.1 shows the general layout of the accelerator.

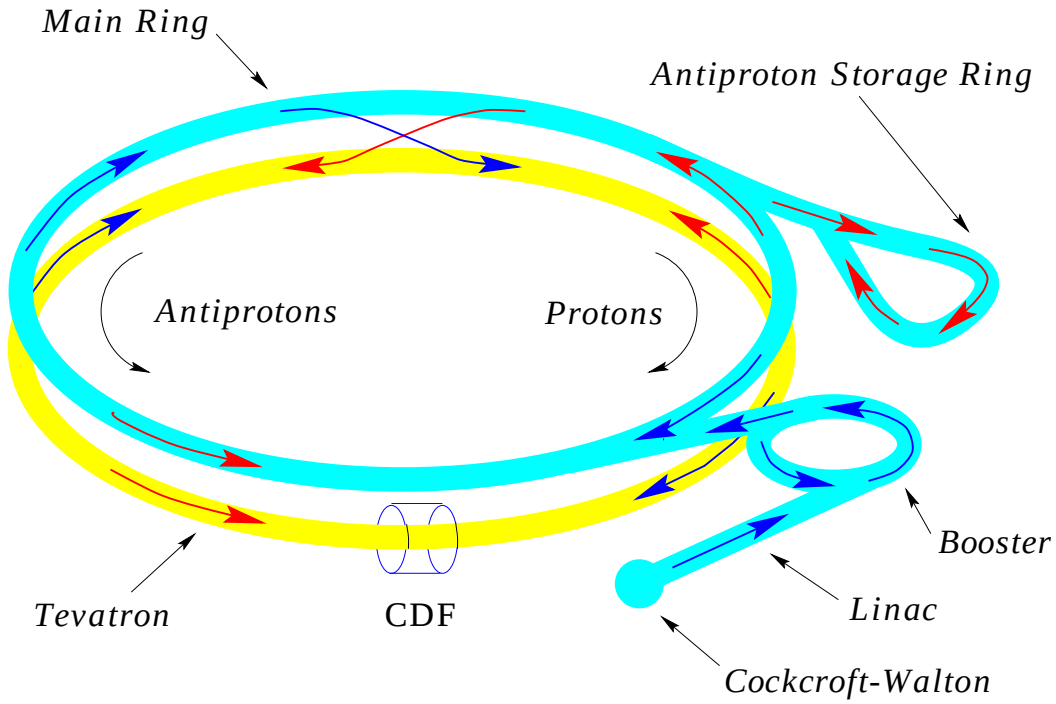

Figure 3.1: Schematic of the Fermilab accelerator complex.

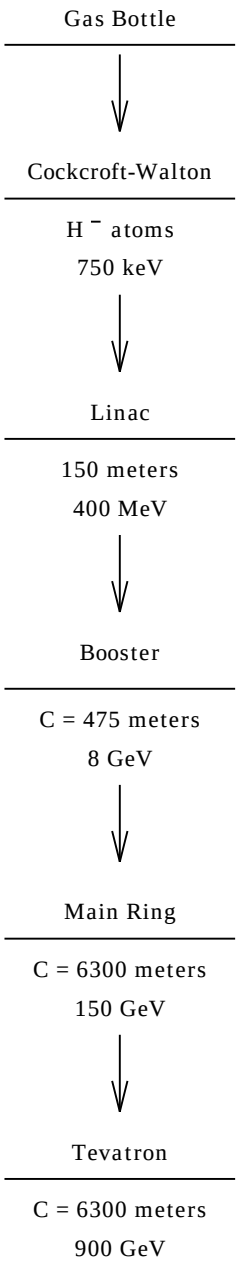

Figure 3.2: Flow chart of the proton's path through the accelerator.

3.1.1 Proton Acceleration

The stages and energies of the proton's path through Fermilab's accelerator process are summed up in Figure 3.2. The process begins with an ion source that produces 18 keV H^- ions from a bottle of hydrogen gas. The ions are injected into a Cockcroft-Walton generator, where they are accelerated through an electric potential drop of 750 keV. The 750 keV ions are then injected into a linear accelerator (Linac), where their speed is increased until they reach an energy of 0.4 GeV.

Linear accelerators are limited by the fact that the beam passes each accelerating cavity only once. To reach higher and higher energies, it becomes practical to bend the beam into a circle, so that it can pass the same accelerating cavities again and again. This is the logic behind the design of proton synchrotrons (circular accelerators), the type of machines that comprise the rest of Fermilab's accelerator complex.

Upon injection into the first synchrotron, the Booster Ring, the beam passes through a thin carbon foil. This foil strips the electrons away from the ions, transforming them into bare protons, or H^+ ions. The proton beam is then accelerated to an energy of 8 GeV. Next, the protons are injected into the Main Ring, which is a proton synchrotron with a radius of 1 km. Here they are accelerated to 150 GeV. The Main Ring is then used to inject protons into the Tevatron. The Tevatron occupies the same tunnel as the Main Ring, so it also

has a 1 km radius. It is the final stage accelerator, and is currently the most powerful particle accelerator in the world. It accelerates the protons to 900 GeV, or 0.9 TeV. This is where the nickname Tevatron is derived — it can accelerate protons to 1 TeV (rounded off) of energy.

3.1.2 Antiproton Acceleration

To produce antiprotons, protons at 120 GeV, rather than the nominal Main Ring energy of 150 GeV, are removed from the Main Ring and focused on a nickel target. The 120 GeV energy was selected as optimally efficient for producing antiprotons. For every batch of 10^{12} protons incident on the target (a typical size for the proton bunches), approximately 10^7 $\bar{p}$'s are eventually collected. As depicted in Figure 3.3, the generated $\bar{p}'s$ are focused with a lithium lens. The resulting parallel beams of $\bar{p}$'s pass through a 1.5 T dipole magnet that selectively deflects negatively charged 8 GeV particles. The 8 GeV $\bar{p}$'s are injected into the Debuncher storage ring at time intervals of 3 seconds. Once in the Debuncher, the antiprotons undergo stochastic cooling to reduce their transverse emittance (i.e., the amount of phase space the particles occupy in the transverse plane), and radio frequency (RF) bunch rotation to reduce their momentum spread. Stochastic cooling refers to a technique of sampling the average location of protons within a bunch, and quickly applying an electric "kick" to the bunch to get the average direction of travel better aligned along the beam pipe. The bunch rotation technique uses RF power to decrease the energy spread of the particles within the

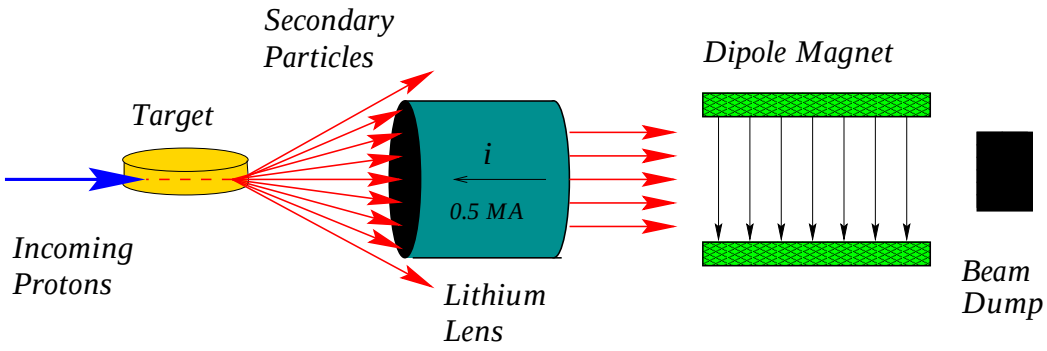

Figure 3.3: Production of antiprotons, at the $\bar{p}$ source.

bunch, while increasing their time spread in order to maintain a constant area in phase space.

The bunches remain in the Debuncher for 2 seconds, during which time they experience successive applications of bunch rotation and stochastic cooling. Then, the partially cooled antiprotons are injected into the Accumulator. In the Accumulator, or Antiproton Storage Ring, they undergo further stochastic cooling and are stored in a rotating "stack" until a sufficient number have been gathered to be injected into the Main Ring for their final acceleration.

3.1.3 Tevatron and Collisions

Six proton bunches are injected into the Tevatron first, and then 6 bunches of antiprotons are extracted from the Accumulator, injected into the Main Ring where they are accelerated to 150 GeV, and then injected into the Tevatron. Because antiparticles have the same mass but opposite charge, charged particles and their

antiparticles automatically move in opposite directions in a magnetic field, so the proton and antiproton bunches are accelerated in the same beam pipe in opposite directions. As viewed from an airplane, the protons travel clockwise around the ring, and the antiprotons travel counterclockwise, as in Figure 3.1. The Tevatron RF cavities accelerate the bunches to 900 GeV, the Tevatron dipole magnets bend the bunches around the circle, and the Tevatron quadrupole magnets focus the bunches more tightly, to increase their density, and hence, increase the beam luminosity. This system of 6 bunches on 6 bunches, creates 12 $p\bar{p}$ intersection points along the ring, carefully tuned to match up with the positions of the particle detectors. (Six of these points are referred to as A0 $\rightarrow$ F0. Originally, the accelerator ran with three proton bunches and three antiproton bunches, and therefore, there were only six collision points.) At these 12 intersection points, the bunches cross every 3.5 microseconds.

When the beams pass each other at these intersection points, the electric attraction between protons and antiprotons perturbs the two beams. This distorts the orbits of the individual particles and causes beam losses, a phenomenon referred to as the beam-beam tune shift. In order to keep the tune shift as small as possible, the intersection points that are not being used for experiments are equipped with electrostatic separator plates. These charged plates separate the two oppositely charged beams in space, minimizing their effect on one another. In Run 1, physics experiments were set up only at points B0 and D0. In the past, and scheduled again for the future, there have also been experiments conducted

at C0.

The low-β quadrupole magnets located around the beam pipe inside the CDF collision hall then squeeze the beam down to increase its density as much as possible in order to maximize the interaction rate. The final step is scraping, which is accomplished by tightening metal collimators around the beam. Scraping reduces the physical size of the beam and decreases the beam halo by eliminating some of the stray protons and antiprotons traveling around the Tevatron at the outer edges of the bunches.

3.2 The Collider Detector at Fermilab

The Collider Detector at Fermilab (CDF) resides at B0, which is one of the points where the Tevatron beams collide. CDF is a general purpose, modular detector designed to analyze the debris produced in high energy $p\bar{p}$ collisions. These debris, or decay particles, enable us to reconstruct particles that were generated in the $p\bar{p}$ collision. For this analysis, the detector was used to measure momenta of muons in the forward region. (As mentioned earlier, the *forward region* refers to the forward and backward regions collectively.) These measurements were then used to reconstruct J/ψ particles. CDF has been described in detail elsewhere [20], so I will simply give an overview of the general features of the detector, and then describe the detector component which recorded and measured forward muon tracks.

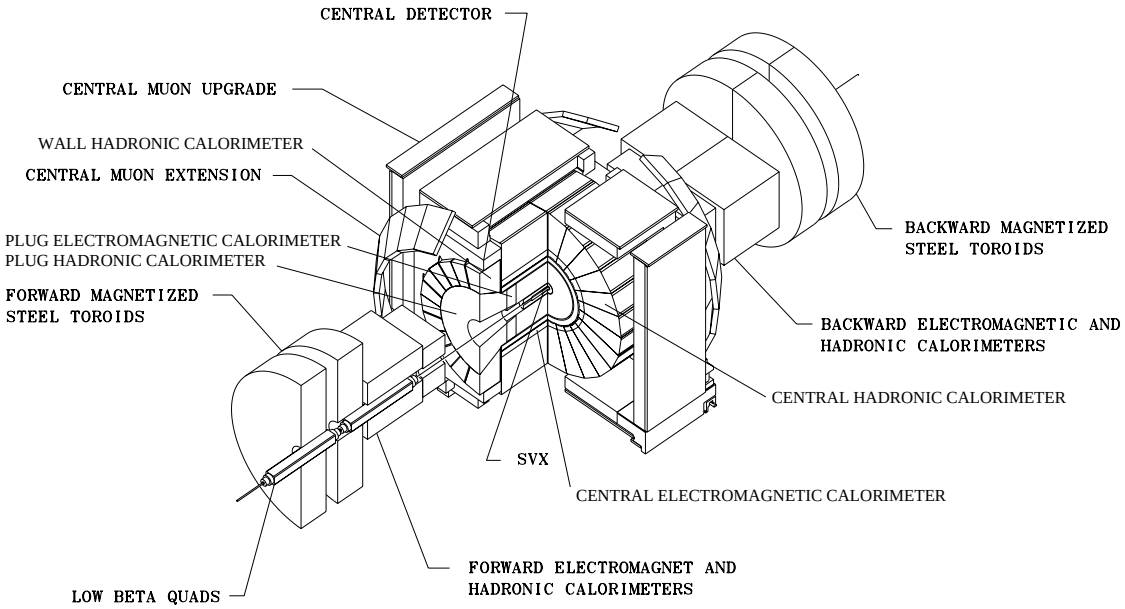

Figure 3.4: Three-dimensional cut-away view of the CDF detector.

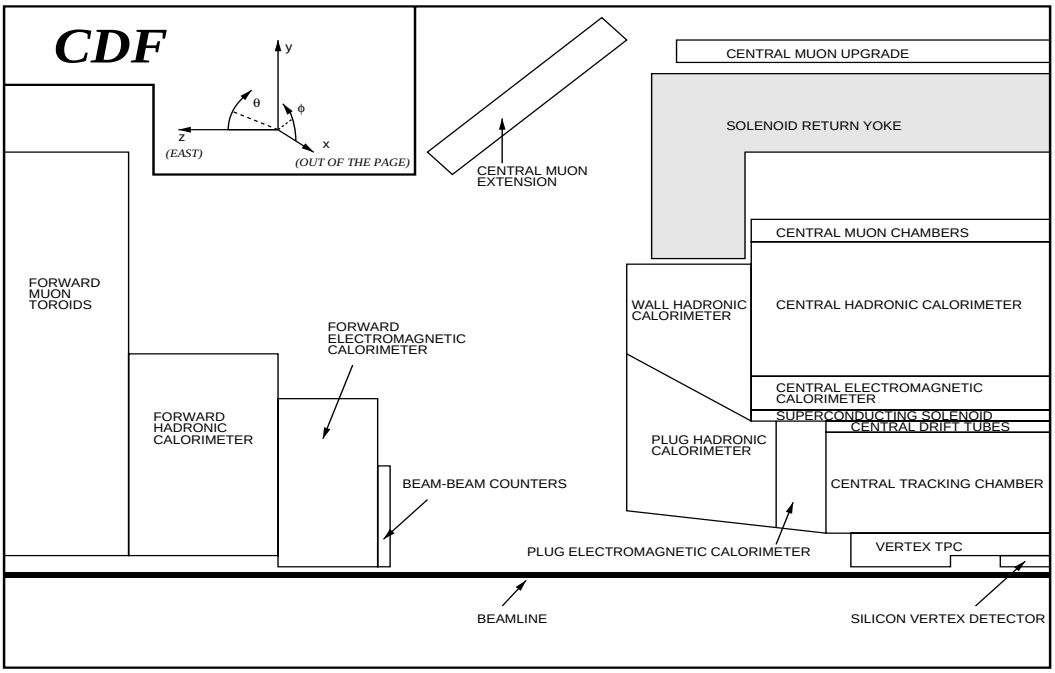

Figure 3.5: Side view of 1/4 of the CDF detector. The interaction region is on the right edge of the figure at the beamline. The detector is forward-backward symmetric and axially symmetric about the beamline.

CDF consists of a central detector comprising tracking, calorimeter, and muon subsystems, and two forward/backward detectors consisting of calorimeters and muon spectrometers. A three-dimensional cut-away picture of the detector is shown in Figure 3.4. Also, in Figure 3.5, there is a side view of one quarter of CDF. The detector is forward-backward symmetric, and most systems are axially symmetric around the Tevatron beampipe, so this view provides a decent picture of the entire detector. In addition, the CDF coordinate system can be seen in the diagram at the top of Figure 3.5.

Coordinates for the collider are defined such that the Z axis is aligned along the proton direction at the interaction point. The X axis points away from the center of the Tevatron Ring, which leaves the Y axis pointing up out of the ground. X_0, Y_0, Z_0, is defined to be the center point of the detector. Azimuth (ϕ) and polar (θ) angles are measured from the X and Z axes respectively, while the cylindrical radius variable r measures perpendicular distance from the beam line. Transverse quantities (p_t, E_t, etc.) refer to projections in the $r-\phi$ plane, i.e., transverse quantities are components which are entirely perpendicular to the beamline. Finally, pseudorapidity, η, is defined as $\eta \equiv -\ln(\tan(\theta/2))$. Pseudorapidity is a convenient variable to express angle with respect to the beam because we expect production of roughly equal numbers of QCD particles for every unit of η. It is also convenient because η, unlike rapidity (y), is independent of mass. For massless particles, pseudorapidity is equal to rapidity.

The Tevatron beam pipe passes through the center of the detector. Charged

particle trajectories are reconstructed in three dimensions using the CDF central tracking system, which consists of three complementary detectors, the Silicon Vertex Detector, the Vertex Detector, and the Central Tracking Chambers, all immersed in a 1.4 T solenoidal magnetic field. The field is generated by a 1.5 m radius solenoid Nb-Ti/Cu superconducting magnet, and enables the measurement of a charged particle's transverse momentum (p_t). The Silicon Vertex Detector (SVX) projects particle tracks back to the beamline, in order to determine a particle's origin. There is a primary vertex from which most tracks stem, and some events also have a secondary vertex from which other tracks stem. These secondary vertices indicate that a massive particle was created in the $p\bar{p}$ collision, moved a small distance, and then decayed. The existence of a secondary vertex, within certain parameters, is a clear signal that a given collision produced bottom quarks. Since the SVX only covered the central region, it provided the ability to identify b quark events in the central region.

Around the SVX is the Vertex Detector (VTX), which functions similarly to the SVX. The VTX also projects particle tracks back to the beamline, but does so to determine the primary vertex. It records the position of the original $p\bar{p}$ collision, in order to establish the event origin of particle tracks recorded elsewhere in the detector.

Located just outside the solenoid, the central calorimeter system consists of electromagnetic (EM) and hadronic (HAD) calorimeters designed to measure the total energy of charged and neutral particles, by stopping them and measuring

the amount of energy they deposit. As mentioned, the forward detectors also house calorimeters. Finally, muon detectors are located beyond the calorimeters in both the central (CMU) and forward (FMU) detectors. Because the muon mass is roughly 200 times the electron mass, muons radiate much less energy than electrons do. In addition, muons do not feel the strong force, and therefore, do not interact strongly with nuclei, as hadrons do. These properties cause muons to be extremely penetrating. To take advantage of this, muon detectors are placed outside the calorimeters, which conveniently shield the muon detectors from most other particles.

In the forward region, at about $10^\circ < \theta < 36^\circ$, and about $144^\circ < \theta < 170^\circ$, the endcaps of the solenoid are layered away from the vertex with the Plug Calorimeters (EM and then HAD) filling the gap. Behind the plug, are the Forward Calorimeters (EM and HAD). Finally, behind these resides the Forward Muon Detector (FMU).

Because of the geometry of colliding physics experiments, the forward and backward detectors are in a noisy area, where the backgrounds to data collection are large. They are located near the beamline, which, when running, is surrounded by a *beam halo* of particles that travel along with the proton and antiproton bunches. These are high energy particles, created by protons/antiprotons brushing against the beampipe. Also, the low-β quadrupole magnet that compresses the beam for collisions, as can be seen in Figure 3.4, is located around the beampipe, just inside of the FMU detector. When the beam halo strikes

this magnet, it can result in a high energy spray that is difficult to distinguish from the actual data. In addition, there is interference from the beams in the Main Ring accelerator, which occupies the same tunnel as the Tevatron. FMU is a physically huge detector component (see the next section for details), and because of it's prodigious size and mass, it acts as a very effective shield for the rest of CDF, protecting it from most of these backgrounds. This shielding effect is intentional, as it helps clean up the data seen by FMU itself.

Great care was taken to clean up the data even more, both as it was being taken, and later in offline analysis. Many of these steps are described in the next chapter.

The detector components used in this analysis are the Forward Muon Detector, and the Vertex Detector. These devices provide us with enough information in each event to identify the position of the collision vertex where the outgoing particles are first produced, and to measure the forward muon momenta. The rest of this chapter details the measurement of muon tracks in the forward detector.

3.3 Forward Muon Detector Components

The Forward Muon (FMU) Detector is a muon spectrometer in the small angle region at CDF, as shown in the cutaway schematic of Figure 3.6. At each end of CDF there are a pair of toroidal magnets (1.5 to 1.8 Tesla field strength) with planes of drift chambers in front, between, and behind. The four toroids

are each made of roughly 100 tons of steel. They are each one meter thick, with an outside diameter of 7.6 meters and an inside diameter of 1 meter. In the front and rear planes, there is a scintillator plane hung outside of the drift chambers and the toroids. Each scintillator plane consists of 24 chamber wedges containing 3 scintillators apiece, as shown in Figure 3.7. In practice, FMU covered a rapidity range of $2.0 < |\eta| < 2.8$. This corresponds to polar angles between $7^\circ < \theta < 16^\circ$ (the forward region), and between $164^\circ < \theta < 173^\circ$ (the backward region). Physically, the detector extended to higher rapidities than $|\eta| = 2.8$, but large backgrounds in the higher rapidity region made data-taking very difficult. It was decided that the trigger region would cover only $2.0 < |\eta| < 2.8$, which helped to prevent beam halo and particles scattering off the low-β magnets from diluting the usable data.

The drift chambers were mounted so they overlapped, however the scintillator chambers were abutted into position. Thus, the active volume of the scintillators contained small gaps near the wedge boundaries, but the drift chambers had no gaps. The specific design parameters for the chambers as well as the survey procedure may be found elsewhere [21, 22]. Instead of concentrating on previously documented dimensions and construction materials, this section describes the general detector design schematically.

As mentioned, there were two chamber types, scintillator and drift. The drift chambers contain a coordinate plane of 56 wire cells and an ambiguity plane of 40 wire cells. For angles in θ greater than 7° (in absolute value), the

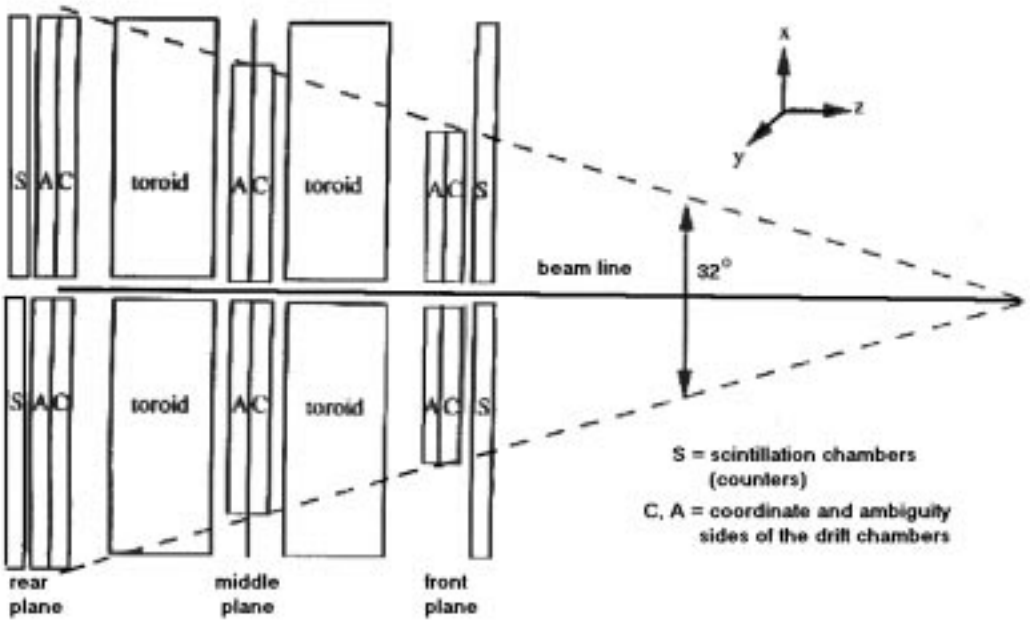

Figure 3.6: Side view of half of the Forward Muon Detector. The detector is symmetric about the vertex.

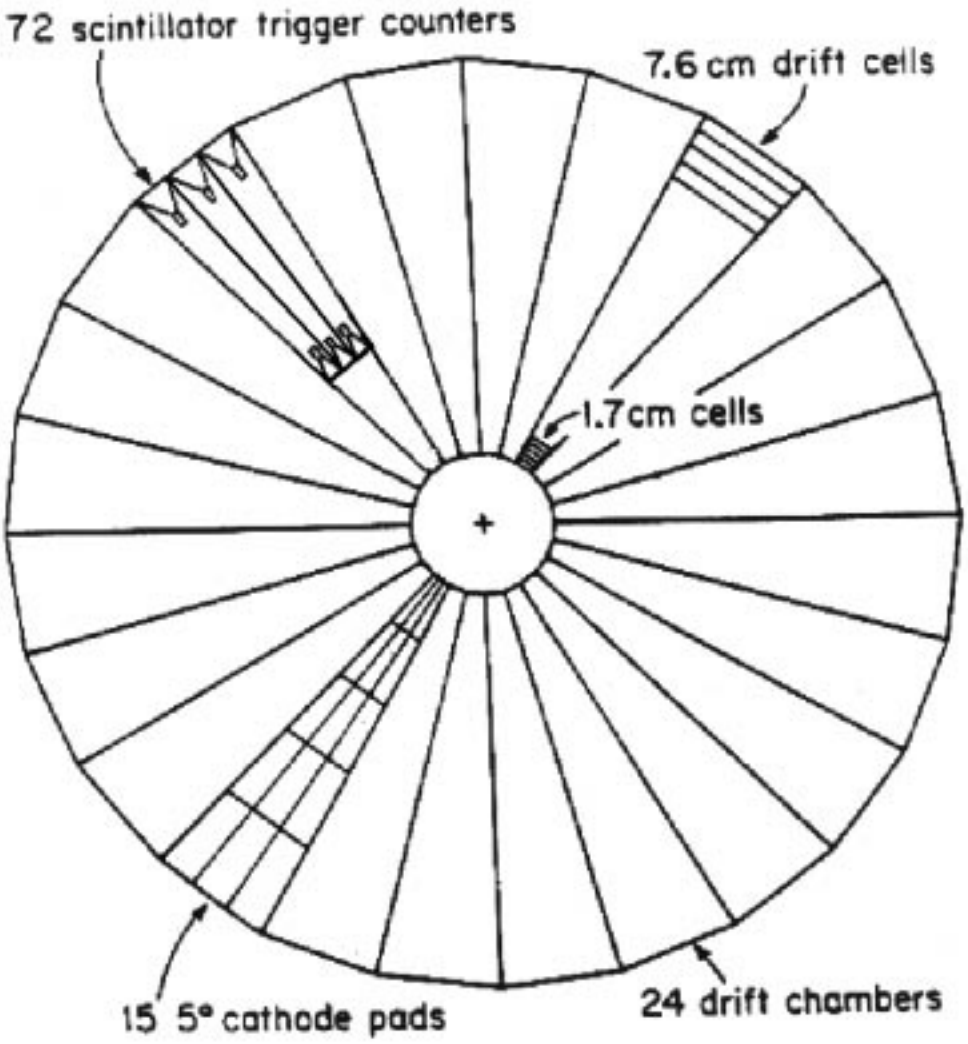

Figure 3.7: Schematic of the FMU chamber and scintillator planes. Each plane consists of 24 chambers, each of which spans 15° in azimuth.

coordinate and ambiguity wires are half cell staggered to resolve the left-right ambiguity. The wires and pads are arranged to form projective towers. The cell size increases with radius such that tracks contained within a projective wire tower correspond to a constant p_t (transverse momentum) threshold. (The specific transverse momentum threshold was determined by the way the Level 1 trigger (see Chapter 4) was written.) The wires were held at high voltage and the pads formed the ground plane between the coordinate and ambiguity sides.

The scintillators were added to FMU after the construction of the wire chambers, to improve the quality of the data. They were included as part of the FMU triggers, to help prevent recording garbage hits as actual data. They were not used in the measurement of muon momenta, but simply confirmed the existence of a muon track. A muon was thus required to have a good quality track in the wire chambers, and also to leave hits in the scintillators and cathode pads that matched up to the chamber track. This was effective in sifting noise from actual muons.

3.3.1 Diagnostics

The forward muon system included diagnostics for many parts of the system. On each scintillator, an LED was mounted which could be pulsed through Fastbus (a hardware control system developed at Fermilab) and read out through the normal data path. In addition, by turning off the voltage to all phototubes in a chamber, except one, each phototube could be individually tested, thus fully

verifying its operation. The diagnostic for the wire chamber consisted of a wire which ran the length of the chamber and coupled capacitively to the sense wires in the chamber. When the long wire was pulsed, the output signals would follow the normal data path. To monitor the gain of the chambers, radioactive iron-55 sources were mounted in four chambers of each plane. Each chamber contained a variety of cell sizes, every different size necessitating a different voltage. An Fe55 source was placed inside one cell of each size, and the signals from the Fe55 sources were used to diagnose overall gain problems.

The gas gain system read out the signals from the Fe55 sources through an emitter follower attached to an alternative output on the pre-amplifier. Since these signals were produced on the chamber and monitored 200 feet away, a significant amount of attenuation occurred in the cable. The chamber high voltages were adjusted to maintain an Fe55 pulse height of 200 $\pm$ 85 mV at the monitoring station, corresponding to 460 mV to 1140 mV as measured at the chamber output [22]. For comparison, a test setup was used to measure the chamber efficiency as a function of the size of the source signals. Figure 3.8 shows how the chamber efficiency depends on the source signals. From this it was concluded that the gas gain was high enough to collect data with 99.6 $\pm$ 0.5 % efficiency, for channels in good working order [23, 24].

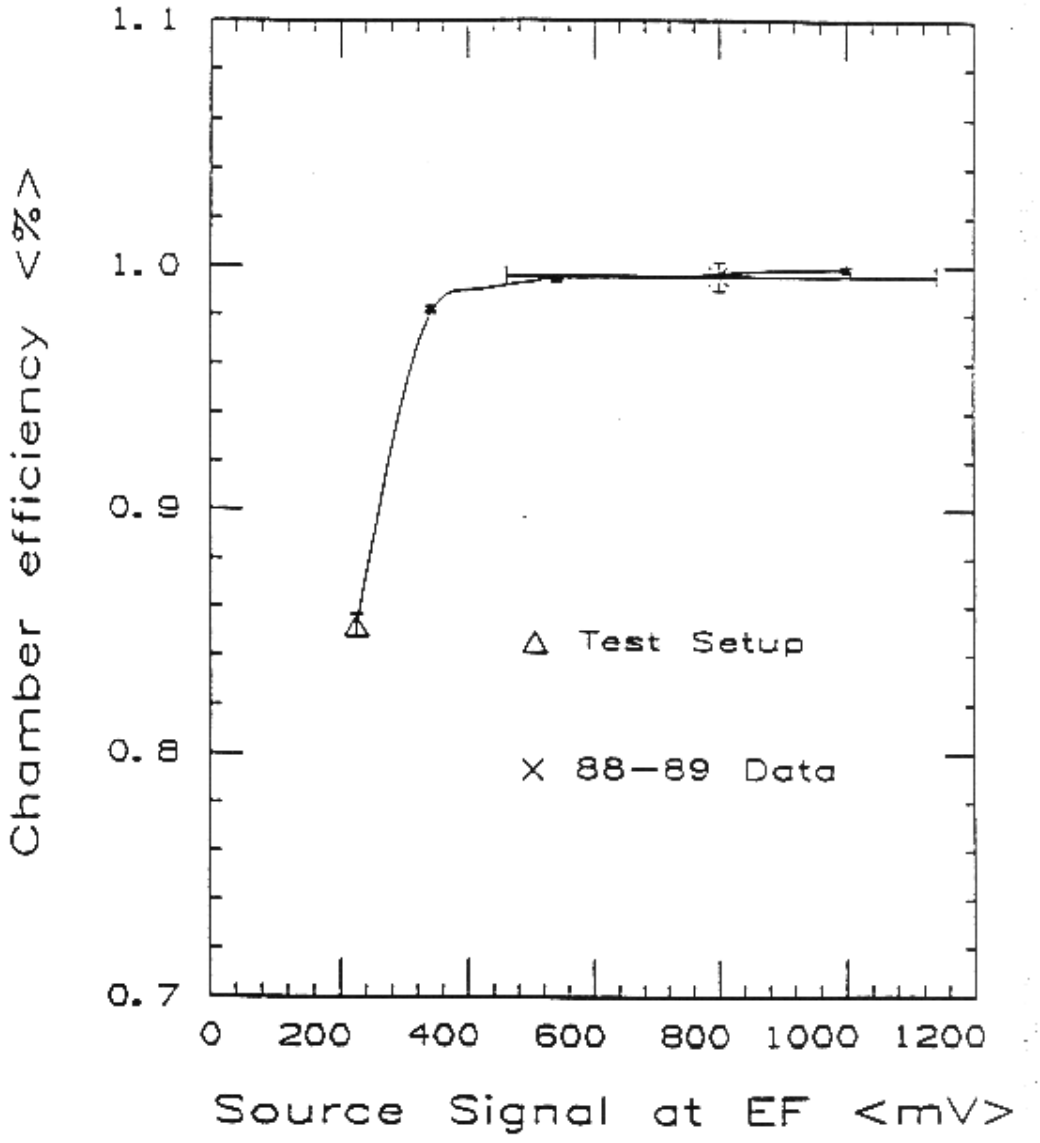

Figure 3.8: Efficiency as a function of gain for the FMU drift chambers. (Taken from Jodi Lamoureux's thesis, *Direct $\bar{b}b$ Production in $\bar{p}p$ Collisions at* $\sqrt{s} = 1.8$ *TeV*, 1993.)

3.3.2 Boosting Chamber Efficiency

Drift chambers are essentially large geiger counters, i.e., they are sense wire chambers that record when a particle travels through the gas that comprises the sensitive volume of the chamber cell. The FMU drift chambers are depicted in Figure 3.9. Each FMU cell has one positive high voltage anode wire running through the center. Charged particles ionize the gas as they pass through the cell, then electrons freed from the gas atoms ionize other gas atoms, and create a cascade of charged particles. The positive ions travel toward the cell wall, and the negative ions travel toward the anode wire. Because the negative ions have much greater mobility than the positive ions do, they reach the anode while the positive ions continue to drift. This net movement of charge induces signals on both the anode sense wire and the pad cathode. The signal on the sense wire is read out as a chamber wire "hit", and the signal on the cathode is seen as a hit in the chamber pads.

Unlike with geiger counters, drift chamber hits are carefully recorded in time, so the precise position of the passing charged particle can be calculated. This calculation is based on the known speed at which ions travel in the cell electric field.

In a sense wire chamber, it is important that the electric field inside the chamber cell be uniform. Sometimes this is accomplished by stringing an intricate pattern of field-shaping wires around the central sense wire. A less complicated

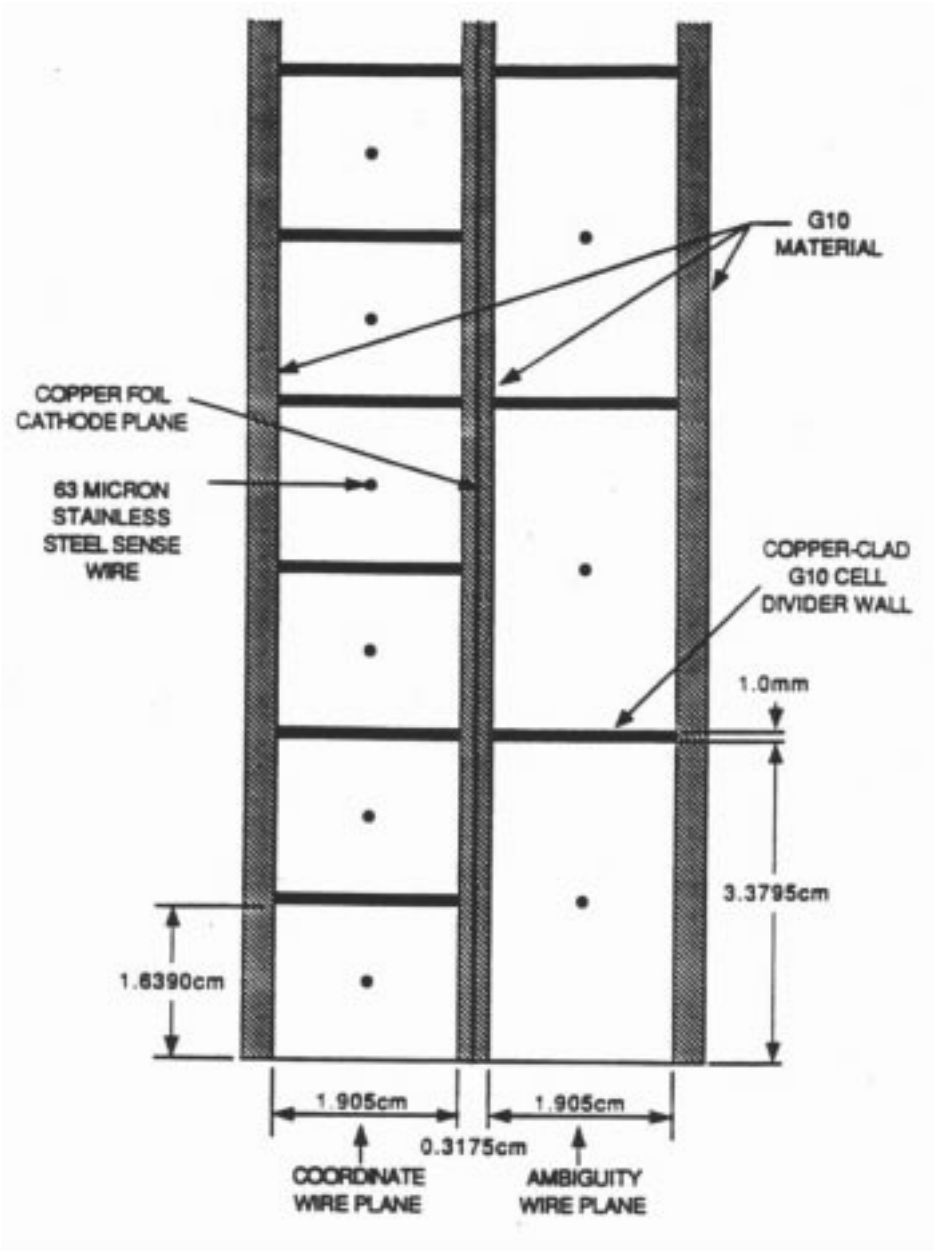

Figure 3.9: Schematic of the FMU chamber cell geometry and materials. The dimensions given are those for the inner radius cells of a front plane chamber.

method, and the one employed in the construction of FMU, is to leave out field-shaping wires, but make the cell walls insulating. This allows gas, ionized by charged particles passing through the cells, to be deposited and to build up on the cell walls. This build-up eventually results in an equilibrium charge distribution on the insulating cell walls, which automatically creates a correctly shaped electric field. At CDF, this build-up was accomplished in a matter of minutes, and occurred just before the start of data-taking.

One of the problems inherent in this more elegant method of sense wire chamber construction, is that although the rate of accumulation of ions on the cell wall decreases after an equilibrium charge distribution is obtained, the accumulation doesn't stop entirely. Eventually, too much charge builds up on the cell wall. This effect decreases the electric field at the sense wire, and hence the gain decreases also.

During Run 1A, two procedures were implemented to help prevent this charge build-up from becoming a problem. The first was to reverse the voltage of the sense wires during the down time between data-taking. Initially, this procedure was performed too rapidly, and the power supplies had problems dealing with the flow of charge out of the detector. This was soon remedied, and the deionization process significantly helped fight charge build-up in the cells.

The second procedure implemented to fight the ionization effect was to increase slowly the voltage of each high voltage sense wire during data-taking. This way, when positive charges on the cell wall decrease the electric field, an

increase in positive voltage on the sense wire would restore it. The amount that the voltages were increased depended on the cell size and the length of time that data-taking continued. For the largest cells, voltages were increased by a maximum of 10% over the course of 24 hours of data-taking.

This procedure was first attempted as an experiment during Run 1A, and before the end of that run, it was implemented as an automated system of voltage increases. FMU data-taking and data quality during Runs 1B and 1C were much improved over Run 1A, and the automated procedure to increase voltages was one of the main reasons why.

3.4 Forward Muon Tracking and Momentum Resolution

A detailed description of the tracking algorithm may be found elsewhere [21, 25]. To reconstruct muon tracks from the chamber hits, a least squares fit was performed using the vertex and 3 hit positions, one at each chamber plane. First, a simple parabolic fit was made. Taking the parameters determined by the parabolic fit as an input, a second, more complicated fit, was performed iteratively. This improved fit included corrections for both multiple scattering and chamber resolution. Finally, a χ^2 value was calculated for each track, to judge the quality of the fit. The square roots of the diagonal covariance matrix elements

for least squares fits are the uncertainties of the fitted parameters.

The momentum resolution of the FMU system has been discussed in more detail elsewhere [23]. It has three components, which are presented here in Table 3.1.

First, there is a momentum uncertainty due to the fact that muons scatter in the forward calorimeters and in the FMU toroids (multiple scattering), which results in hits that are randomly distributed around the ideal track positions. Second, as in any measuring device, there is a contribution to the uncertainty of the measurement from the inherent resolution of the detector (chamber resolution). And, finally, the third contribution to the momentum resolution comes from uncertainties in the chamber positions due to the limitations of the survey used to determine those positions [26].

When the contributions from each of the sources listed in Table 3.1 are combined, the momentum resolution is given by:

$$\Delta P/P = \sqrt{(.166)^2 + (.0019P/\ \text{GeV})^2}. \tag{3.1}$$

As we will see in chapter 5, the FMU momentum resolution was well-modeled by the detector reconstruction software — indicating that it is well understood.

Momentum Resolution Factors	$\Delta P/P$
Multiple Scattering	$.166 \pm .004$
Chamber Resolution (650 microns)	$(.0015 \pm .0003) \times P$
Survey Uncertainties	$(.0012 \pm .0003) \times P$

Table 3.1: Sources contributing to the momentum resolution.

Chapter 4

Data

4.1 Trigger

At the Tevatron, $p\bar{p}$ collisions occur at a rate of 285 kilohertz, but CDF was only capable of recording data events at a maximum rate of 6 Hz. Therefore, one of the biggest challenges to CDF, and in fact, to all high energy collider experiments, is to sift through the available data to pick out the events that are the most interesting, so only those data get saved. At CDF, this is accomplished by a three stage *trigger*, or filter, that combines both hardware and software elements. The stages of the trigger are referred to, in the order they are applied, as Level 1, Level 2, and Level 3.

When designing a trigger, one first decides what characteristics mark an interesting event. Some characteristics are always considered interesting: very high

energy decay products usually mark an event where a massive object was created, a clean electron pair or muon pair often marks an event that can be reconstructed easily, and is therefore useful, etc. However, triggers are also written for specific analyses. The analysis that is the subject of this thesis relied on events where two muons were detected in the forward region.

A vital consideration to making a good measurement is that different triggers are active for a different amount of time, and therefore, for a different amount of data-taking. Obviously, an analysis has to keep careful track of the amount of data recorded; there must be some way of counting the number of collisions for which a specific trigger is live.

The quantity that high energy physicists measure to record the size of a data set is called Luminosity, $\mathcal{L}$. It's a quantity that is proportional to the intensity of the particle beam, hence the name. Instantaneous luminosity, L, is defined in terms of measurable characteristics of the beam:

$$L = fn\frac{N_1 N_2}{A} \tag{4.1}$$

where f is the rotation frequency of the beam, n is the number of bunches of protons and antiprotons (assuming that the number is the same for both — which is true at the Tevatron), N_1 is the number of protons per bunch, and N_2 is the number of antiprotons per bunch, and A is the cross sectional area of the beam.

Instantaneous luminosity is then integrated over the time for which a given

trigger is active, to yield luminosity:

$$\mathcal{L} = \int L \, dt. \tag{4.2}$$

The units for luminosity are 1/area.

4.1.1 FMU Dimuon Trigger

The triggers which are relevant to this analysis have been described in more detail elsewhere [27, 28]. The data for this analysis were taken with the FMU Level 3 dimuon trigger, MUOB_FMU_DIMUON_V1. The trigger required a set of drift chamber and scintillator hits consistent with the geometry expected of a high-p_t muon originating from the nominal interaction point, at the center of the detector. The trigger required two reconstructed forward muon tracks, each with $p_t > 4.5$ GeV/c and with $\chi^2 < 20$. Each track required 6 (out of a possible 6) hits in the FMU wire chambers. To reduce background, events were rejected if either FMU octant containing a track had more than 40 hits total. Also, there was a requirement that there be a road of 3 pad hits plus 2 scintillator hits. This road was required to be in the same octant as the wire hit track. If there were two muons in the same octant, a single pad-scintillator road could satisfy the requirement. However, if two muons were in different octants, each one had to satisfy the pad-scintillator road independently.

The trigger was rate limited to 0.6 Hz. In Run 1B, this limit was rarely invoked, because of the dimuon trigger's intrinsically low rate. However, in Run

1C, the data acquisition channel through which the dimuon trigger was read out was combined with the channel for the single forward muon trigger readout. This was done to free up a channel for other analyses. The single forward muon trigger had a much higher rate than the dimuon trigger did, so the combined triggers were affected much more strongly by the rate limit. This effect was partially offset by the fact that Run 1C had a lower average instantaneous luminosity than did Run 1B.

4.1.2 Luminosity

The luminosity measurement for this analysis was provided by Lummon, CDF's program for monitoring beam intensity during data collection. CDF measured luminosity using the beam-beam counters (BBC). These consisted of two planes of concentric rings of scintillator placed symmetrically east and west about the interaction point, between the forward detectors and the central detectors. After extensive study, it was determined that the uncertainty in the luminosity measurements is 4.1%. This uncertainty is due largely to the 3.3% error in the normalization of the BBCs [29].

For good runs only, i.e., for all data-taking runs where there were no mechanical problems, the CDF detector as a whole recorded a maximum luminosity of $71.2 \pm 2.9\ pb^{-1}$ (inverse picobarns) in Run 1B, and $6.9 \pm 0.3\ pb^{-1}$ in Run 1C. Combined, that gives a total luminosity of $78.1 \pm 3.2\ pb^{-1}$ for all of the good runs in both Runs 1B and 1C.

This is more than a factor of 4 times the luminosity of $17.0 \pm 0.7\ pb^{-1}$ recorded by CDF in all of Run 1A (1992-1993). This impressive increase in luminosity is due to the fact that the Fermilab accelerator was running at a much higher rate in Runs 1B and 1C (1994-1995). Specifically, the Tevatron had on average a much larger number of particles per bunch than it did in Run 1A.

The luminosity seen by the forward dimuon trigger was calculated by summing the numbers reported by Lummon files on a run by run basis, which took into account the data lost to the rate limit. In Run 1B, MUOB_FMU_DIMUON_V1 saw a total luminosity of $57.5 \pm 2.4\ pb^{-1}$, and in Run 1C, it saw a total luminosity of $4.2 \pm 0.2\ pb^{-1}$. Combined, the forward dimuon trigger saw a luminosity of $61.7 \pm 2.5\ pb^{-1}$ in all of the good runs in Runs 1B and 1C.

This is roughly a factor of 7 times the luminosity of $8.6 \pm 0.4\ pb^{-1}$, recorded by the forward dimuon trigger in all of Run 1A. This was, of course, partly due to the improvement in the operations of the Tevatron. The rest of the increase was due to the improved operation of the forward muon chambers. Operating FMU in Run 1A served as an excellent detector shakedown. Many mechanical repairs were made over the course of the run, which resulted in a much more robust machine for Runs 1B and 1C. Also, the new procedure for systematically boosting the chamber high voltages (described in Section 3.3.2), was implemented at the end of Run 1A. This procedure improved chamber efficiencies throughout 1B and 1C.

4.1.3 Trigger Efficiency

The FMU single muon trigger efficiency was measured from a study of FMU–CMU Z events. This sample consisted of events with both a good CMU (central muon) and a good FMU (forward muon), which reconstructed a Z. Events that came in on a CMU trigger were checked for the fraction that also passed the FMU trigger. This efficiency was measured at 70%.

The single muon trigger requirement consists of a 6 hit track, plus a pad and scintillator road in the same octant. The efficiency of wire hits for an individual wire, obtained from a study of 5 hit versus 6 hit tracks, is 98%, and is included in the detector simulation. The total efficiency for a 6 hit road, then, is $(0.98)^6 = 89\%$. Therefore, the remaining single muon efficiency is 79% (i.e., $0.7/(0.98)^6 = 0.79$).

The difference between total efficiency in the data, and efficiencies in the monte carlo simulations, is due to the pad-scintillator road required by the trigger, a requirement which is not included in the simulations. When two muons are in different octants, both muons must satisfy the pad-scintillator roads independently, so the two muon efficiency is $(0.79)^2 = 62\%$. When the two muons are in the same octant, either muon can satisfy the pad-scintillator component of the trigger for the event, so the probability of a good pad road becomes $1 - (0.21)^2 = 96\%$. Therefore, the efficiency of a dimuon event satisfying the pad-scintillator road is:

$$\epsilon_{pad-scint} = \frac{N_{same} \cdot (0.96) + N_{different} \cdot (0.62)}{N_{same} + N_{different}} \tag{4.3}$$

where N_{same} is the number of muon pairs that are in the same octant, and $N_{different}$ is the number of pairs where the muons were in different octants.

For this analysis, the data had 1262 same octant muon pairs, and 795 different octant muon pairs, so the monte carlo results have to be multiplied by $\epsilon_{pad-scint} = 83 \pm 4.3\%$ to correct those results to the data. This efficiency agrees with the efficiency calculated from monte carlo yields of same and different octant J/ψs.

4.2 Offline

The data set was created from events that were written to tape using the forward dimuon trigger. This was a very time-sensitive procedure, as each event had to be read out in a matter of milliseconds, so the detector could then be used to look for the next event. After that occurred, several steps were performed offline, with the luxury of time, to improve the quality of the data set. Then, a number of quality cuts were made on the data, in order to throw out noise and high background events.

4.2.1 Retracking

After passing the Level 3 forward dimuon trigger, and being recorded to tape, the FMU data were retracked offline. Each track was refit to the hits that were recorded in the event, so as to give the lowest χ^2 track possible, i.e., the best possible fit to the chamber hits. In addition to the wire hits, the event vertex was used in each fit. Since it is not possible at CDF to identify the event vertex that matches a given forward muon track, the event vertex was obtained by simply taking the first vertex listed in the Vertex Detector's (VTX) data bank. This method was found to select the wrong vertex about 20% of the time, a conclusion based on a study of Z bosons that decayed to a forward muon and a central muon. (In CDF, central muon tracks can be extrapolated back to a vertex. When the central muon vertex was compared to the first VTX data bank vertex, they differed 20% of the time, in this study.)

Because different possible vertices were separated by centimeters, or tens of centimeters, and the vertex and the beginning of the FMU track were separated by about 10 meters, choosing the wrong vertex actually has a fairly small effect on an FMU track measurement. Nevertheless, it was modeled in the detector simulation for this analysis (see Chapter 5).

4.2.2 Analysis Cuts

The Run 1B and 1C data set had 18,415 FMU dimuon pairs in the mass window from 2.0 GeV/c^2 to 4.4 GeV/c^2. 11,780 were opposite sign events, and 6635 were like sign events. Of these events, 4,280 opposite sign events, and 498 like sign events passed the FMU dimuon trigger. Several cuts were employed to improve the quality of these data:

1. Each event was required to satisfy the FMU dimuon trigger.
2. There was a p_t requirement of greater than 5 GeV/c on one muon, and greater than 2 GeV/c on the second muon. This cut was largely redundant with the trigger requirement of 4.5 GeV/c and 4.5 GeV/c, but not completely, partly because of the possibility of a third muon in triggered events.
3. χ^2 for each reconstructed muon track was required to be less than 11.6. This is equivalent to requiring χ probability to be greater than 2%. Ideally, this requirement should pass 98% of the signal events, but it was shown [26] that this cut has an efficiency of $88.7 \pm 0.1\%$ for forward muons.
4. There was a p_t requirement of 10 GeV/c on the parent of the muon pair. Below this point, the correction to the acceptance of the FMU detector becomes large, magnifying the errors.

5. The muon parent (the reconstructed J/ψ) was required to have a pseudorapidity of $2.1 < |\eta| < 2.6$. This requirement eliminated the detector rapidity boundaries, where the acceptance was low.

6. The two muons were required to be separated by either a distance in ϕ of greater than 0.1 radian, or a distance in pseudorapidity of greater than 5 chamber wires (about 0.09 in η). This was required to reduce the chance of confusion, and to avoid double counting chamber hits, in the track reconstruction. This cut forced tracks to be in separate chamber pads, which has the added benefit of simplifying the calculation of the dimuon trigger efficiency.

After these cuts, we were left with 2,143 opposite sign dimuon pairs in the mass window 2.0 GeV/c^2 to 4.4 GeV/c^2, and 86 like sign pairs. When we subtract the like sign background from the data, we are left with 2057 ± 47 events.

With statistics this low, there is a limit to the number of manipulations to which the data can be subjected. There is also a limit to how finely the data set can be divided. However, there is a more than adequate number of events to calculate the inclusive cross section.

Chapter 5

Simulations

5.1 Detector Reconstruction

Several different monte carlo programs were used to model the data. The results from each program were run through FSIM, a fast simulation model of the FMU detector, written by Chris Wendt [26]. However, there were a few elements added to FSIM as part of this analysis. These elements account for previously unmodeled sources of error.

FSIM propagates a simulated muon from the event vertex through the detector (through the chambers, through the toroid steel, etc.). It determines which chamber wires in the detector should have recorded a hit, and records the time of each hit. FSIM outputs these chamber hits, which are then reconstructed into muon tracks. The reconstructed tracks are then required to satisfy the same

Level 1 trigger road as the data, albeit without a pad-scintillator requirement. These tracks were then subjected to all of the quality cuts to which the data were subjected.

In addition to detector geometry, FSIM models the effects of the FMU toroid magnetic field, multiple scattering and energy loss in the FMU toroids, survey errors on the FMU geometry, an incorrect event vertex in the tracking 20% of the time (see Section 4.2.1), and extra chamber hits from delta rays and muon bremsstrahlung.

FSIM also models the effect of the central solenoid magnetic field on dimuon events. The solenoid field pushes a forward muon slightly to one side as it travels through the central detector. For two oppositely charged muons, this either increases or decreases the opening angle between them, depending on the orientation of their charges with respect to the magnetic field. Since the opening angle enters directly into the calculation of the mass of the muons' parent, the solenoid field directly affects the measurement of the J/ψ mass. On average, this effect leaves the overall mass measurement unchanged, but it increases the width of the mass peak.

5.2 B Decays

Originally used to verify the FSIM detector reconstruction, a simplified monte carlo was written by Lee Pondrom to simulate J/ψs from B decays. This pro-

gram was subsequently found to reproduce the forward J/ψs better than existing monte carlo packages. It used the momentum distribution for the B meson measured in the CDF central region [30], and the B rapidity distribution used was obtained from ISAJET. It forced the decay $B \rightarrow \psi + X$, using the psi momentum distribution in the rest frame of the B meson, as measured by CLEO [31]. It then used simple kinematics to decay the ψ to two muons.

CDF has previously measured an inclusive cross section in the central region of B mesons decaying to J/ψs plus unspecified other objects ($B \rightarrow J/\psi + X$). This measurement used events which found two muons in the Central Muon chambers, and was thus restricted to pseudorapidities of -0.6 to 0.6. It also required that each reconstructed J/ψ have a transverse momentum greater than 10 GeV/c. In addition, the central measurement did something a forward measurement can not do; it used CDF's Silicon Vertex Detector (SVX) to identify B mesons in each event. Therefore, it is known that these central J/ψs came from B meson decays, and the cross section measurement excludes directly produced J/ψs. This previous measurement provides us a known cross section, which we can use to normalize monte carlo results that come from B decays.

The central J/ψ analysis measured an exclusive cross section of:

$$\sigma(B \rightarrow J/\psi \rightarrow \mu\mu,\ \psi_{p_t} > 10\ GeV/c,\ |\eta| < 0.6) = 256\ \pm\ 51\ pb\ [14]. \qquad (5.1)$$

Pondrom's $B \rightarrow \psi$ monte carlo produces a yield of 20,614 dimuon events with $|\eta| < .6$, and $\psi_{p_t} > 10$ GeV/c. Using the measured cross section, the simulation

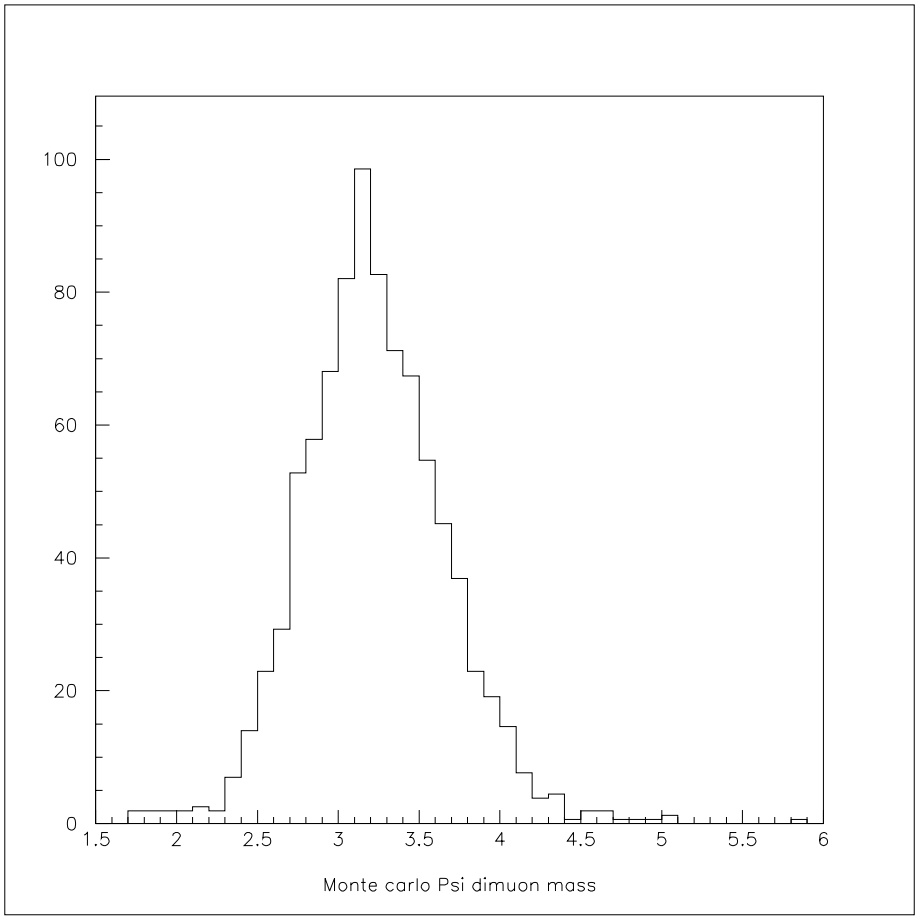

Figure 5.1: Calculated $B \rightarrow \psi + X$ signal, plotted in GeV/c^2.

result corresponds to an integrated luminosity of:

$$\mathcal{L} = \frac{20,614}{256\ pb} = 80.5\ \pm\ 16.1\ pb^{-1}. \tag{5.2}$$

For $2.1 < |\eta| < 2.6$, the $B \rightarrow \psi$ monte carlo generated 8,374 dimuon events, putting them in the geometric region of the FMU chambers. Of those, 2,143 events survived the detector reconstruction in the range $1.5\ GeV/c^2 < M_{muon\ parent} < 6.0\ GeV/c^2$, and 1,389 survived all of the quality cuts of the analysis. In the mass range of interest, $2.0\ GeV/c^2 < M_{muon\ parent} < 4.4\ GeV/c^2$, there were 1,367 events after all cuts. When that result is normalized to the $62\ pb^{-1}$ of the data, we are left with:

$$N_{events} = (1389)\frac{61.7\ pb^{-1}}{80.5\ pb^{-1}}(0.83) = 883\ \pm\ 188 \tag{5.3}$$

or in the mass region of interest

$$N_{events} = (1367)\frac{61.7\ pb^{-1}}{80.5\ pb^{-1}}(0.83) = 869\ \pm\ 185 \tag{5.4}$$

where the error is dominated by the uncertainty in the B cross section. In this calculation, a correction factor of 83% has been included to account for the efficiency of the pad-scintillator road requirement, since the pad-scintillator road is the one component of the overall trigger efficiency which has not been included in the simulations before this point. This result is plotted in Figure 5.1.

5.3 Drell-Yan Background

One of the most common types of events at high energy colliders is a class of interactions known as Drell-Yan events. First described by Sidney Drell and Tung-Mow Yan in 1970 [32], these occur when a quark and an antiquark annihilate each other in the initial collision, producing a quantum of energy (a photon), which then results in the creation of a particle and its antiparticle partner, also known as pair production. An example of these interactions is shown in Figure 5.2. Since the dimuon sample consists of oppositely charged muons (i.e., a muon and an antimuon), Drell-Yan events that produce a muon pair will be a background to any dimuon analysis.

To model this background, and also to calculate the cross section of Drell-Yan events (so that the background can be normalized to the data), a program written by HEP phenomenologists Dieter Zeppenfeld, Tao Han, and Jim Ohnemus was used. The program output was fed into FSIM, and then into the same analysis module that was run on the data.

This program generated Drell-Yan events using a next-to-leading order expansion in α_s of the production cross section. Because of the expansion in α_s, this program did not calculate the K factor of the Drell-Yan cross section, which also depends on α_s [33]:

$$K = 1 + \frac{4\alpha_s}{2\pi \cdot 3}\left(1 + \frac{4}{3}\pi^2\right) \tag{5.5}$$

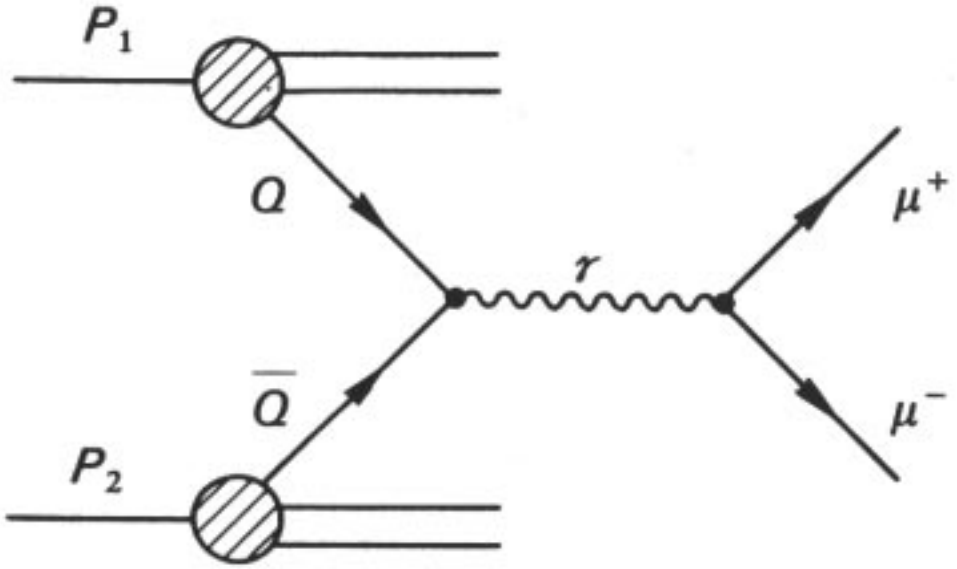

Figure 5.2: Diagram showing production of a photon (γ), and the decay to a muon pair, from a quark-antiquark collision (the Drell-Yan process).

where

$$\alpha_s(Q^2) = \frac{12\pi}{(33 - 2f)\ln(Q^2/\Lambda^2)} \tag{5.6}$$

However, if we take Λ = 0.2 GeV (A free parameter that must be determined experimentally; it has been shown to be between 200 MeV and 250 MeV [34].), f = 5 (the number of quark flavors)[1], and Q = 10 GeV (because we require $\psi_{p_t} > 10$ GeV/c), a straightforward calculation gives $K = 1.6$.

The Drell-Yan monte carlo calculated a production cross section of $33 \pm 7\ pb$, for events that generate two forward muons. This calculation assumed a K factor of 1. Our "back of the envelope" calculation computed K = 1.6, so the cross section becomes $(1.6)(33\ pb) = 53\ \pm\ 11\ pb$ for these Drell-Yan events. The program yields 28,714 forward dimuon events before any cuts, which corresponds to a luminosity of:

$$\mathcal{L} = \frac{28,714}{53\ pb} = 542\ \pm\ 108\ pb^{-1}. \tag{5.7}$$

In the region $2.1 < |\eta| < 2.6$, the Drell-Yan monte carlo generated 18,200 dimuon events. Of those, 3,640 events survived the detector reconstruction in the range $1.5\ GeV/c^2 < M_{muon\ parent} < 6.0\ GeV/c^2$, and 2,527 survived all of the analysis quality cuts. In the mass range of interest, $2.0\ GeV/c^2 < M_{muon\ parent} < 4.4\ GeV/c^2$, there were 1,561 events after all cuts. After normalizing to 62 pb^{-1},

[1]Top quarks are too massive to contribute appreciably to this process.

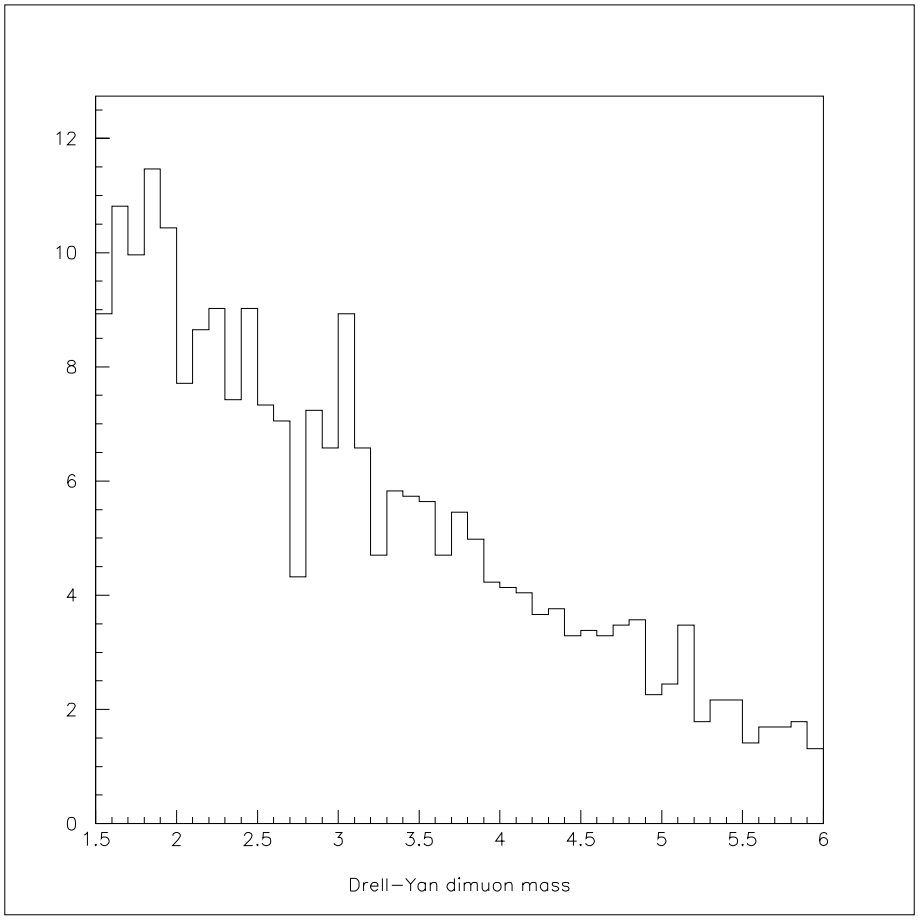

Figure 5.3: Calculated Drell-Yan background, plotted in GeV/c^2.

we have:

$$N_{events} = (2527)\frac{61.7\ pb^{-1}}{541.8\ pb^{-1}}(0.83) = 239\ \pm\ 51 \tag{5.8}$$

where again, a correction factor of 83% has been included for the efficiency of the pad-scintillator road requirement. In the mass region of interest, there are

$$N_{events} = (1561)\frac{61.7\ pb^{-1}}{541.8\ pb^{-1}}(0.83) = 147\ \pm\ 31. \tag{5.9}$$

This result is plotted in Figure 5.3.

5.4 Sequential Decays Background

Finally, we asked, what other physics events would contribute significantly to the dimuon background? There are events where a massive object can decay into something lighter, plus a muon, and then the "something lighter" can decay into a muon and other objects. These are referred to as sequential decays, and if the two muons are opposite in charge, these decays can appear as a background in the dimuon sample. The sequential decay, $B \rightarrow \mu + D$ and then $D \rightarrow \mu + K$, produces oppositely charged muon pairs from B decays with a branching ratio of roughly 0.6% [1], which dominates all remaining physical dimuon processes in the mass region of interest. In this decay, which is pictured in Figure 5.4, B represents a meson with a bottom quark in it. Specifically, it stands for any one of these four mesons: $B^+ = u\bar{b}$, $B^0 = d\bar{b}$, $\bar{B}^0 = \bar{d}b$, or $B^- = \bar{u}b$. D represents a class of mesons with a charm quark, so it stands for any one of these four mesons:

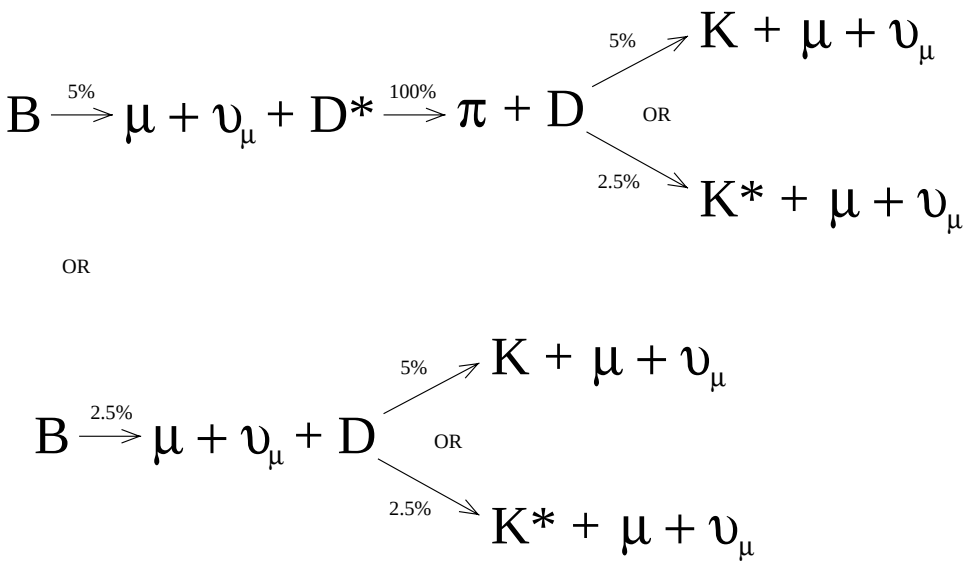

Figure 5.4: Possible sequential decays from the B meson.

$D^+ = c\bar{d}$, $D^0 = c\bar{u}$, $\bar{D^0} = \bar{c}u$, or $D^- = \bar{c}d$. K represents a class of mesons with a strange quark, any one of: $K^+ = u\bar{s}$, $K^0 = d\bar{s}$, $\bar{K^0} = \bar{d}s$, or $K^- = \bar{u}s$. The D could also be a D^*, which is one of the previously named D mesons in an excited state. Similarly, the K could be a K^*, which is one of the K mesons in an excited state.

To model this decay, another monte carlo was written by Pondrom that, again, used the CDF B momentum distribution, and the B rapidity distribution from ISAJET. This simulation modeled the dominant B sequential decay. The B meson was decayed in its rest frame to a muon, a D^* meson, and a muon neutrino. The D^* meson was then decayed to a D meson and a pion. Finally, the D meson was decayed to a muon, a K meson, and a muon neutrino.

This monte carlo modeled the dominant decay, out of several possible decay chains, and the results were normalized using the inclusive branching ratio for B sequentials. This is a reasonable approximation to the combination of all possible final states, given the large parent mass. In other words, the 5 GeV/c^2 mass of the B meson dominates the decay kinematics, so all of the final states should behave similarly.

We can not use the central J/ψ analysis to normalize the monte carlo results from B sequential decays, since those sequential decays do not involve J/ψs. Instead, we use the central measurement of the B cross section itself. This cross section [30] used the same data as the central J/ψ analysis, but included monte carlo results which made it possible to correct the measurement to a larger rapidity region, and made it possible to determine the reconstructed B meson transverse momentum.

The central B cross section used data from a pseudorapidity region of -0.6 to 0.6, but used monte carlo results to increase that coverage to the pseudorapidity region between -1.0 and 1.0. Also, for consistency with our forward analysis, we require that the reconstructed B mesons have transverse momenta greater than 10 GeV/c. This requirement yields a cross section of:

$$\sigma(B,\ B_{p_t} > 10\ GeV/c,\ |\eta| < 1.0) = 520\ \pm\ 52\ nb\ [30]. \qquad (5.10)$$

To compare this cross section to the sequential decay, we multiply it by the branching ratio for a B meson to decay to a D, or a D^*, plus a muon, and then

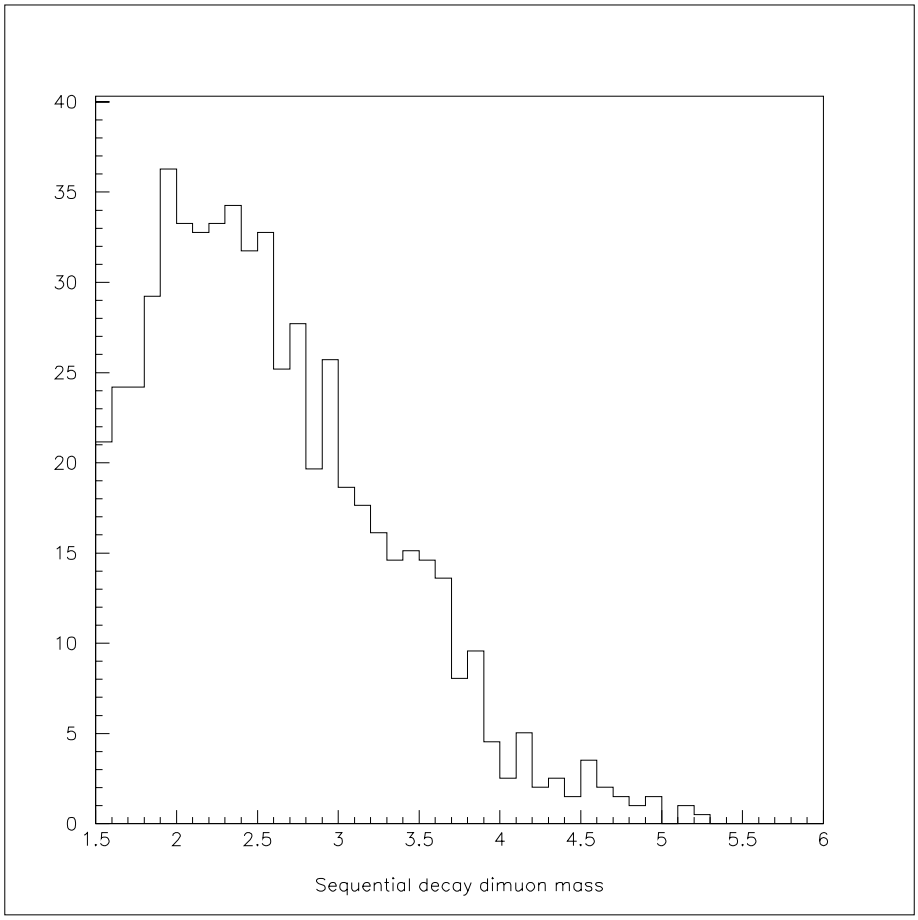

Figure 5.5: Calculated background from muon pairs in sequential B decays, plotted in GeV/c^2.

multiply by the branching ratio for a D meson to decay to a K, or a K^*, plus a muon.

As mentioned before, the B meson can decay into either a D meson and a muon and a muon neutrino, or a D^* meson (an excited state D) and a muon and a muon neutrino. The D^* decays into a D 100% of the time, so these two decays lead to the same final states. The branching ratios are roughly $B \rightarrow D + \mu + X = 2.5\%$ [1], and $B \rightarrow D^* + \mu + X = 5\%$ [1]. If we combine these two decays as equals, we get a branching ratio of $B \rightarrow D \; or \; D^* + \mu + X = 7.5\%$, with an uncertainty of roughly 10%.

The two largest possible decays for the D meson involving a muon are decays to a K meson, plus a muon, plus a muon neutrino, or to a K^*, plus a muon, plus a muon neutrino. These have branching ratios of roughly $D \rightarrow K + \mu + X = 5\%$ and $D \rightarrow K^* + \mu + X = 2.5\%$, with an uncertainty of about 10%. Combining these two branching ratios gives

$$\mathcal{B}\left(B \rightarrow D \; or \; D^* + \mu + X; \; D \rightarrow K \; or \; K^* + \mu + X\right) = 0.0056 \pm 0.0012 \quad (5.11)$$

for the possible sequential decays.

We find that the cross section for the sequential decay is

$$\sigma = (520 \pm 52 \; nb)(0.0056 \pm 0.0012) = 2.9 \; \pm \; 0.6 \; nb. \quad (5.12)$$

Running our monte carlo yields 629,694 dimuon events with $|\eta| < 1$, and $B_{p_t} > 10$

GeV/c. This result corresponds to an integrated luminosity of:

$$\mathcal{L} = \frac{629,694}{(2)(2900\ pb)} = 108.6\ \pm\ 24.3\ pb^{-1}. \tag{5.13}$$

where the factor of two must be introduced because the B meson cross section was measured for b quarks only, and excluded $\bar{b}$ quarks. Since the charge of the quark is unimportant to the monte carlo, this cross section must be doubled to get the correct normalization.

In the region $2.1 < |\eta| < 2.6$, the sequential decay monte carlo generated 376,855 dimuon events, where both muons strike the FMU detector. Of those, 1,750 events survived the detector reconstruction in the range $1.5\ GeV/c^2 < M_{muon\ parent} < 6.0\ GeV/c^2$, and 1,168 survived all of the analysis quality cuts. In the mass range of interest, $2.0\ GeV/c^2 < M_{muon\ parent} < 4.4\ GeV/c^2$, there were 875 events after all cuts. After normalizing to $62\ pb^{-1}$, we have:

$$N_{events} = (1,168)\frac{61.7\ pb^{-1}}{108.6\ pb^{-1}}(0.83) = 551\ \pm\ 130. \tag{5.14}$$

Or, for $2.0\ GeV/c^2 < M_{muon\ parent} < 4.4\ GeV/c^2$,

$$N_{events} = (875)\frac{61.7\ pb^{-1}}{108.6\ pb^{-1}}(0.83) = 412\ \pm\ 97. \tag{5.15}$$

Figure 5.5 shows this result.

5.5 Comparison to the Data

Figures 5.6 and 5.7 show the monte carlo results superimposed on the data. In Figure 5.6, each result is plotted separately, and Figure 5.7 shows the results

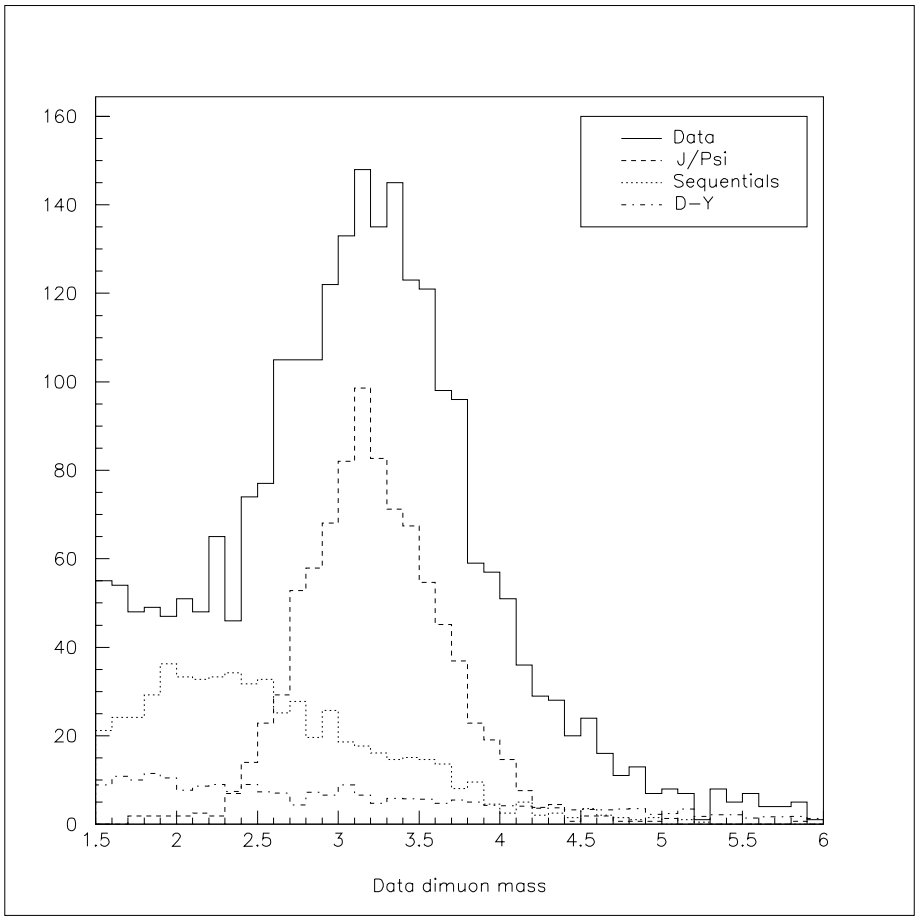

Figure 5.6: Monte carlo results superimposed on the data, plotted in GeV/c^2. The data are drawn as a solid line, and each monte carlo is a separate dotted line.

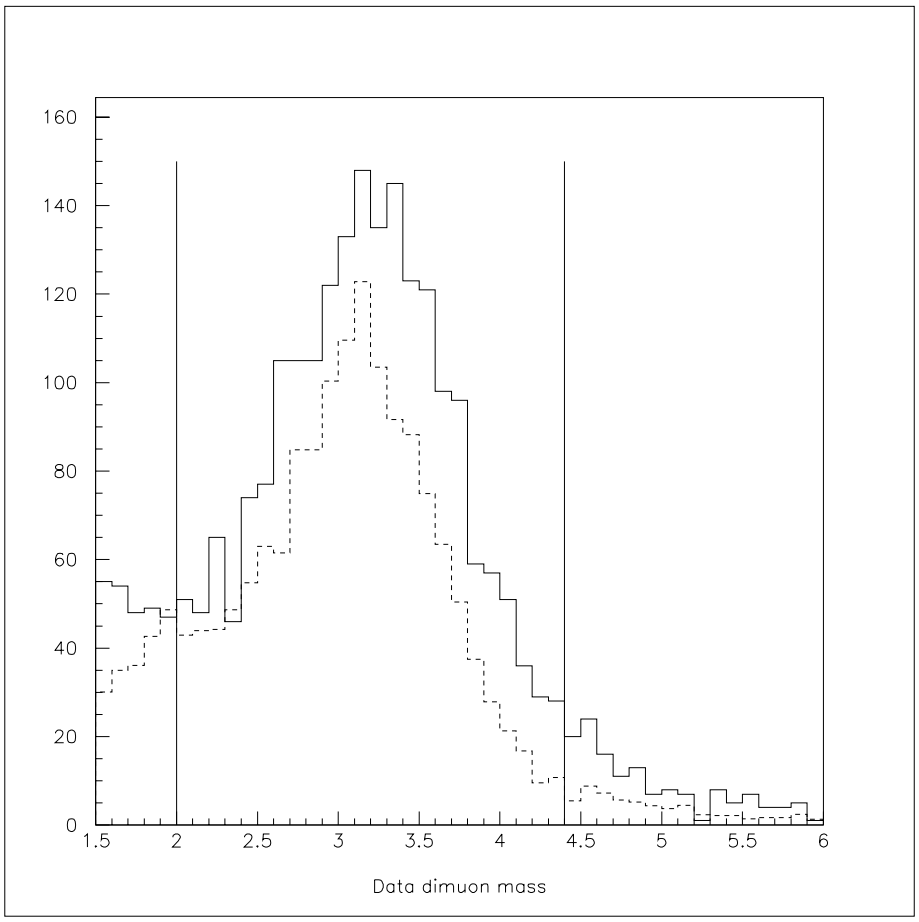

Figure 5.7: Monte carlo results superimposed on the data, plotted in GeV/c^2. The dotted line is the sum of the three monte carlo results. The vertical lines were added to show the region of interest.

combined. On both plots, the data are represented by the solid line, and monte carlo results are drawn with dotted lines. The combined simulations do a fair job of reproducing the shape and magnitude of the background, and the shape of the signal. The fact that the monte carlo results are lower than the data in the signal region ($2.0\ GeV/c^2 < M < 4.4\ GeV/c^2$) is probably due to the fact that no prompt component of J/ψ production was modeled.

One conclusion we can draw is that the monte carlo simulations used here reproduce the backgrounds and the shape of the data well in the region of interest. This serves to verify not only the data models, but also the FSIM detector reconstruction.

Chapter 6

Cross Section Calculation

6.1 Fitting the Monte Carlos

Thus far, I have presented comparisons of the data to monte carlo expectations, to which no adjustments have been made. This has been done to illustrate qualitatively how close the data are to our naive expectations of J/ψs from B decays. However, all of the monte carlo calculations used in this analysis share one flaw; they are theoretical calculations that have never been verified experimentally. This is a consequence of working in the forward region of a collider detector. Since measurements have so rarely been made in the forward direction, there are insufficient data to verify even starting assumptions in the monte carlo programs. For example, even Pondrom's simplified simulations rely on either the B cross section, or the J/ψ cross section, as measured at CDF in the central

region. As discussed in Sections 2.7 and 2.8, there are strong theoretical reasons to assume that those cross sections will be different in the forward region.

In order to obtain a quantitative cross section, the background must be more accurately obtained. This will be done by taking the known components of the signal and the background, previously discussed, and fitting them to the data mass distribution.

For this study, in order to match the backgrounds more accurately, a low mass background component was also modeled. Decays of light quark mesons such as the ρ, ϕ, and η mesons were included in the fit. These decays add a small mass peak, which is centered around 1 GeV/c^2. The inclusion of this expected decay did not affect the signal area, but it improved the quality of the background fit.

A four-parameter fit was performed, which adjusted the relative heights of the simulated J/ψ peak, the Drell-Yan events, the sequential decays, and the light meson decays, until they fit the shape of the data distribution. The region of fit extends from a mass of 1.5 GeV/c^2 to 6.0 GeV/c^2. The results of that fit are shown in Figures 6.1 and 6.2. The fit has a χ^2 value of:

$$\chi^2 = 30.2/41\ dof = 0.74/dof. \tag{6.1}$$

Table 6.1 and Table 6.2 show the changes made by the four parameter fit. In Table 6.1 the naive expectations from the previous chapter are listed in the first column. For each monte carlo, the number of events that survived all analysis cuts after normalizing to 62 pb^{-1}, are given. The second column lists the number of

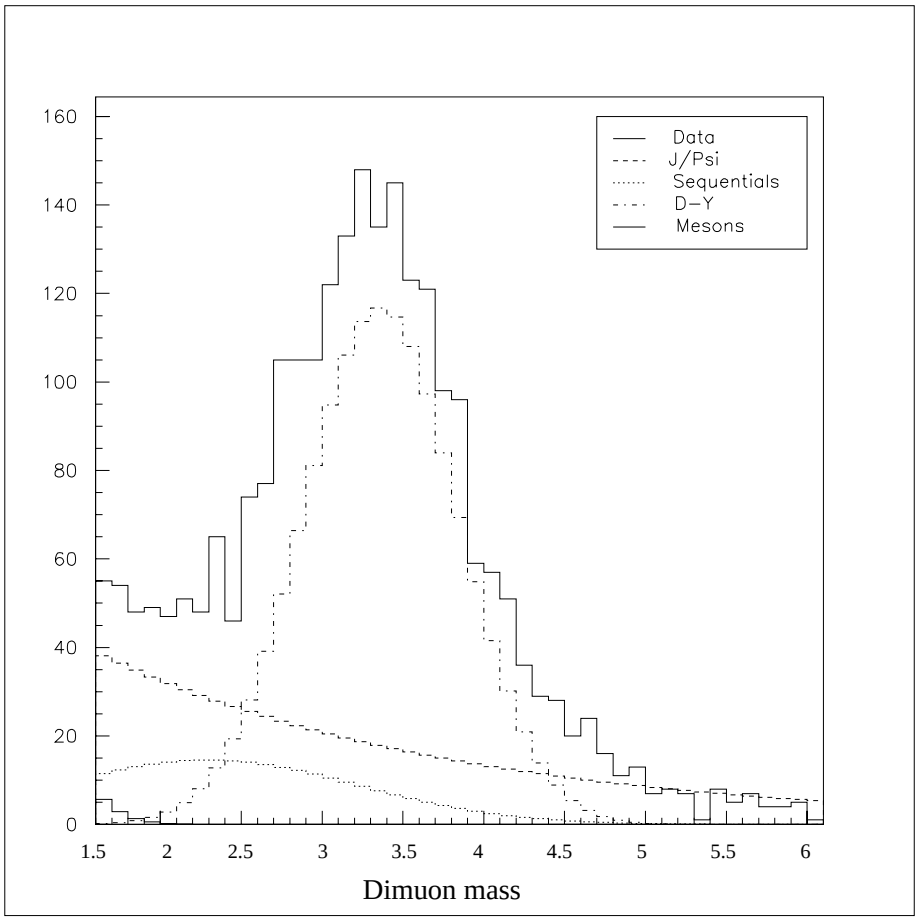

Figure 6.1: Results of the four parameter fit, plotted in GeV/c^2. Each monte carlo is drawn as a separate dotted line. The dotted lines are superimposed on the data (solid line).

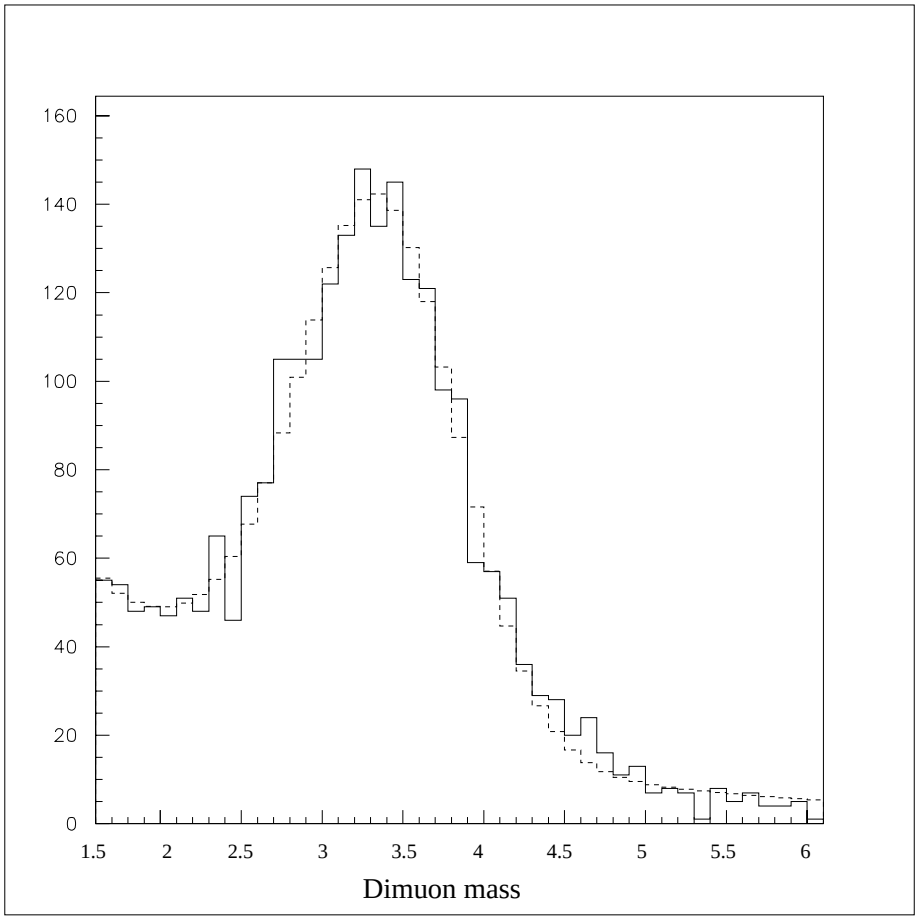

Figure 6.2: The dotted line is the sum of the four fitted monte carlo results. They are superimposed on the data, and plotted in GeV/c^2.

	Unfitted events in 62 pb^{-1}	Fitted number of events
Data	2451 $\pm$ 52	2451 $\pm$ 52
$B \rightarrow J/\psi$	883 $\pm$ 188	1405 $\pm$ 45
Sequentials	551 $\pm$ 130	263 $\pm$ 41
Drell-Yan	239 $\pm$ 51	757 $\pm$ 44
Light Mesons		11 $\pm$ 11

Table 6.1: Comparison of the fitted results to the unfitted results in the region 1.5 $GeV/c^2 < M_{dimuons} < 6.0\ GeV/c^2$.

	Unfitted events in 62 pb^{-1}	Fitted number of events
Data	2057 $\pm$ 47	2057 $\pm$ 47
$B \rightarrow J/\psi$	869 $\pm$ 185	1387 $\pm$ 45
Sequentials	412 $\pm$ 97	195 $\pm$ 31
Drell-Yan	147 $\pm$ 31	460 $\pm$ 27
Light Mesons		0.1 $\pm$ 0.1

Table 6.2: Comparison of the fitted results to the unfitted results in the region 2.0 $GeV/c^2 < M_{dimuons} < 4.4\ GeV/c^2$.

events calculated from the fit in the same region, for each monte carlo. Table 6.2 displays the same information, except that all of the numbers are for the mass region of interest ($2.0\ GeV/c^2 < M < 4.4\ GeV/c^2$). This table includes the numbers that will be used for the cross section calculation.

As we can see from Table 6.2, the fitted result for Drell-Yan events is more than three times our original expectation, suggesting that we have underestimated this background. Also, the result for the sequential decay background is about one third of our naive expectation, which suggests that we have overestimated the number of b quark events in our data, possibly by as much as a factor of three. We can also see that the fitted result has more ψ events than we expect. This, most likely, would be prompt J/ψ events, which were not modeled at all.

Figure 6.3 shows the signal events alone, after the background events, as determined by the four parameter fit, have been subtracted. After removing 655 ± 41 background events,

$$N_{signal} = N_{data} - N_{sequentials} - N_{Drell-Yan} = 2057 - 195 - 460 = 1402 \pm 61. \quad (6.2)$$

there are 1402 ± 61 signal events left in the mass window from $2.0\ GeV/c^2$ to $4.4\ GeV/c^2$. The data distribution is centered on a mass of $3.2\ GeV/c^2$, with a standard deviation of 0.56. So, the $2.4\ GeV/c^2$ mass window is two standard deviations wide on either side of the mean, and centered on the mean of the distribution.

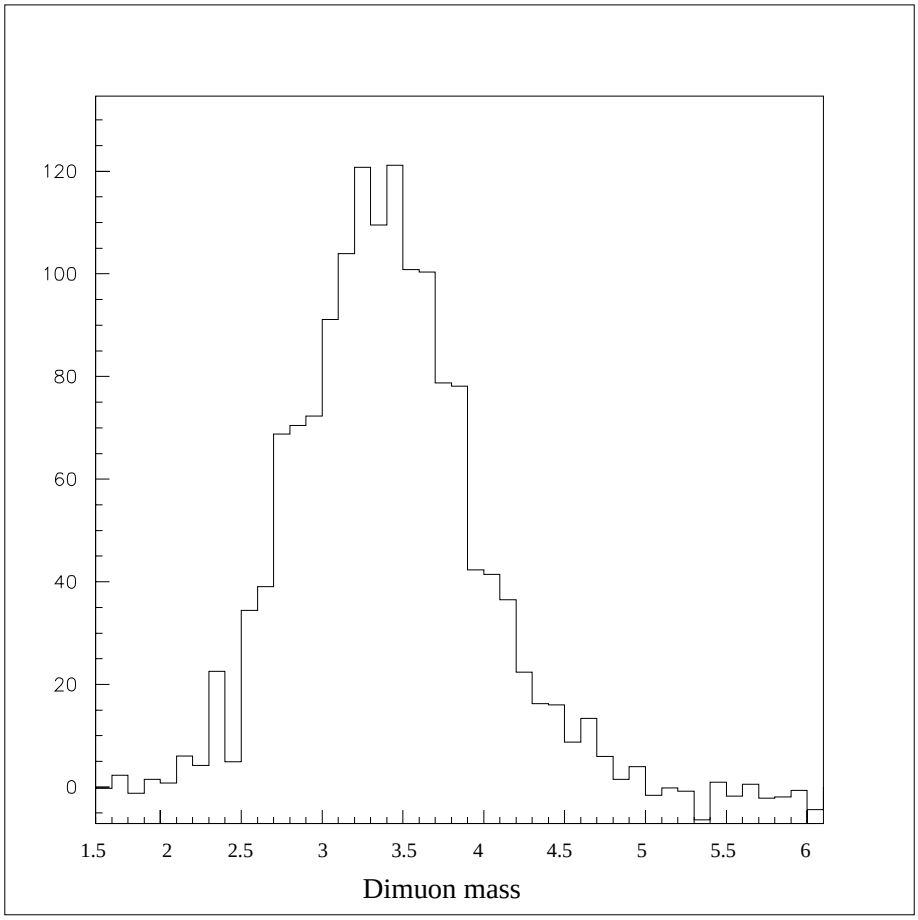

Figure 6.3: Signal events after subtracting backgrounds, plotted in GeV/c^2.

6.2 Cross Section

A cross section is computed from the equation:

$$\sigma = \frac{N_{events}}{\epsilon \cdot \mathcal{L}} \tag{6.3}$$

where N_{events} represents the number of events in the signal region (after background subtraction), $\mathcal{L}$ is the luminosity of the data sample, and ϵ is the total efficiency.

In this analysis, there were 1402 ± 61 dimuon pairs in the data after subtracting all of the background events. Since this analysis required the forward muon dimuon trigger, the correct value for $\mathcal{L}$ is the luminosity seen by that trigger, or $61.68 \pm 2.53\ pb^{-1}$.

The total efficiency can be calculated from the simulations. Every known source of error in the FMU detector is reproduced in the FSIM detector reconstruction, with the sole exception of the scintillator-pad requirement in the trigger (see Section 4.1.3). Therefore, the total efficiency is calculated by dividing the number of generated $J/\psi \rightarrow \mu^+ \mu^-$ events that passed the detector reconstruction and all analysis cuts, by the total number of generated $J/\psi \rightarrow \mu^+ \mu^-$ events in the appropriate geometric area (i.e., the events where both muons would strike the FMU detector). Then, this number is multiplied by the scintillator-pad efficiency, and by the η range that the FMU detector subtends.

$$\epsilon_{TOT} = \frac{N_{events\ \ that\ pass}}{N_{generated\ events}} \epsilon_{pad-scint} F_{\eta\ range} \tag{6.4}$$

Pondrom's $B \rightarrow \psi$ monte carlo produces $8,374 \pm 92$ dimuon events where the J/ψ has $2.1 < |\eta| < 2.6$, $p_t > 10\ GeV/c$, and each muon has $1.9 < |\eta| < 2.8$, which requires both muons to strike the FMU. Of these events, $1,367 \pm 37$ events survive the detector reconstruction and all of the analysis cuts. The scintillator-pad efficiency was calculated as $83 \pm 4.3\%$, and the analysis requires the muon parent particle to have $2.1 < |\eta| < 2.6$, for an eta range of 1. Therefore,

$$\epsilon_{TOT} = \frac{1,367}{8,374}(0.83)(1.0) = 13.5 \pm 0.8\% \tag{6.5}$$

the total FMU efficiency for events that pass the dimuon trigger is 13.5%.

Therefore, the inclusive cross section for forward J/ψs per unit η at CDF is:

$$\sigma = \frac{1,402}{(0.135)(61.68)} \tag{6.6}$$

or

$$\sigma(J/\psi \rightarrow \mu\mu,\ \psi_{p_t} > 10\ GeV/c,\ 2.1 < |\eta| < 2.6) = 167.8 \pm 14.2\ pb. \tag{6.7}$$

6.3 Cross Section as a Function of Transverse Momentum

With 1402 events, there is a limit to the number of manipulations that can be performed on the data, but they can be split up somewhat. They can, for example, be separated into several different p_t bins.

Dividing the data into p_t bins gives the results in Table 6.3 and Table 6.4. In Table 6.3, the first column lists the average transverse momentum of the bin (5 GeV/c width, starting at 10 GeV/c). Since the data fall off with increasing p_t, the average p_t per bin is smaller than the p_t at the center of the bin. The second column is the number of data events in each bin. Columns three, four, and five calculate the efficiency for each bin, in the same manner as it was calculated in the previous section. Column three lists the number of events generated in each bin by Pondrom's $B \rightarrow \psi$ monte carlo. Column four lists the number of $B \rightarrow \psi$ events in each bin which pass the detector reconstruction and all analysis cuts. Column five divides the two numbers, and then multiplies the result by the 83% efficiency for satisfying the pad-scintillator road requirement, which is the only requirement not reproduced in the detector reconstruction. Column six lists the error in the calculation of the efficiency.

Table 6.4 shows the calculation of the cross section for each p_t bin. The first two columns again list the average transverse momentum of the p_t bin, and the number of data events in each bin. Column three shows the result of dividing the data by the efficiency. Column four lists the actual cross section, and column five shows the error in that calculation.

In order to calculate the cross section, because the data in column two (either table) do not have the backgrounds subtracted, the data are multiplied by 0.682, the fraction of signal events to total events. This gives us the number of signal events in each bin. Then, the data over ϵ ratio is divided by the luminosity, and

Average P_t	Data Events	Generated ψ Events	Accepted ψ Events	$\epsilon_{\psi\ events}$	$\epsilon_{\psi\ events}$ error
11.7	1476	6470	788	0.1011	$\pm$0.006
16.7	430	1456	403	0.2297	$\pm$0.018
21.7	108	341	124	0.3018	$\pm$0.035
26.7	31	87	39	0.3721	$\pm$0.074
31.7	10	16	7	0.3631	$\pm$0.166
36.7	2	4	6	1.245	$\pm$0.806

Table 6.3: J/ψ data and efficiencies versus p_t.

Average P_t	Data Events	Data/ϵ	$d\sigma/dp_t$ $(pb/GeV/c)$	$d\sigma/dp_t$ error $(pb/GeV/c)$
11.7	1476	14599	32.27	$\pm$2.46
16.7	430	1872	4.14	$\pm$0.36
21.7	108	358	0.79	$\pm$0.10
26.7	31	83	0.18	$\pm$0.04
31.7	10	28	0.06	$\pm$0.03
36.7	2	2	0.004	$\pm$0.004

Table 6.4: J/ψ cross section versus p_t.

the width of the p_t bin:

$$\frac{d\sigma}{dp_t} = \frac{N_{total} \cdot f_1}{\epsilon \cdot \mathcal{L} \cdot F_{bin\ width}} \tag{6.8}$$

where $\mathcal{L} = 61.68\ pb^{-1}$, $F_{bin\ width} = 5\ GeV/c$, ϵ is listed in Table 6.3, and

$$f_1 = \frac{N_{signal}}{N_{total}} = \frac{1402}{2057} = 0.6816 \pm 0.02. \tag{6.9}$$

These results are plotted in Figure 6.4.

The p_t independence of the ratio f_1 was studied by dividing the data into two p_t regions: $10\ GeV/c < p_t < 13\ GeV/c$, and $p_t > 13\ GeV/c$. These ranges each included half of the data. The four parameter fit to the data and then the background subtraction were performed separately on the two different ranges. The resulting ratios for signal events to the total data were

Low p_t range: $f_1 = 0.70 \pm 0.03$

and

High p_t range: $f_1 = 0.68 \pm 0.03$.

6.4 Fraction of J/ψ Events from B Decays

As stated before, we are forced to leave this as an inclusive cross section measurement. The only clue we have regarding the size of the B contribution (versus prompt production) is the calculation of the size of the background contribution from B events, i.e., the sequentials background. As listed in Table 6.2, the fitted

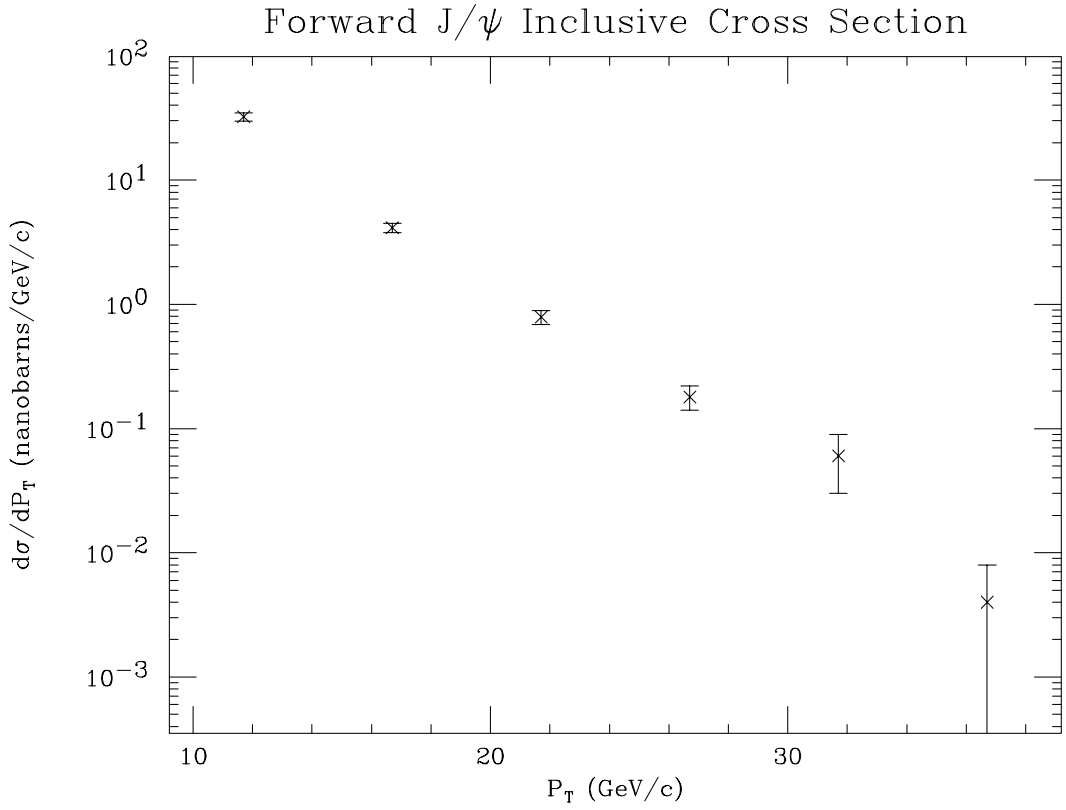

Figure 6.4: The forward muon J/ψ cross section, plotted as a function of p_t.

background of the sequential events is less than half of the unfitted expectation. This suggests that the value for the B cross section measured in the central region is larger than the actual value in the forward region.

If we assume that the fitted background reflects the accurate value of the B cross section, than we can scale our monte carlo prediction for J/ψs from B mesons:

$$\frac{N_{fitted\ sequentials}}{N_{unfitted\ sequentials}} \cdot N_{J/\psi} = \frac{195}{412} \cdot (1387) = 656 \pm 187. \tag{6.10}$$

From that it follows that the fraction of ψs from Bs is:

$$f_B = \frac{N_{B\to\psi}}{N_{total\ \psi}} = \frac{656}{1387} = 0.47 \pm 0.13 \tag{6.11}$$

which is consistent with the fraction measured in the central region.

There are problems with this technique. First, it is based on a fit to the background, rather than any direct measurement. Second, the assumption that the difference between the unfitted results and fitted results is due to a different B cross section does not explain the change between the unfitted and fitted Drell-Yan numbers; there could be some unknown effect which has not been taken into account.

In conclusion, the forward J/ψ yield can not be reliably separated into B and prompt components. However, there is circumstantial evidence that the ratios obtained in the central region may hold here as well.

Chapter 7

Conclusion and Comparisons

This thesis has already compared the forward muon J/ψ cross section to theoretical expectations. The next question of interest is: How does this cross section measurement compare to experimental values of the J/ψ cross section measured previously? This chapter makes those comparisons.

7.1 Comparison to the CDF Central Cross Section

Figure 7.1 compares the forward muon J/ψ cross section to the CDF central measurement [14]. Both inclusive cross sections, calculated with J/ψ transverse momentum greater than 10 GeV/c, are plotted as a function of detector pseudorapidity. The CDF central result was published for a p_t requirement of

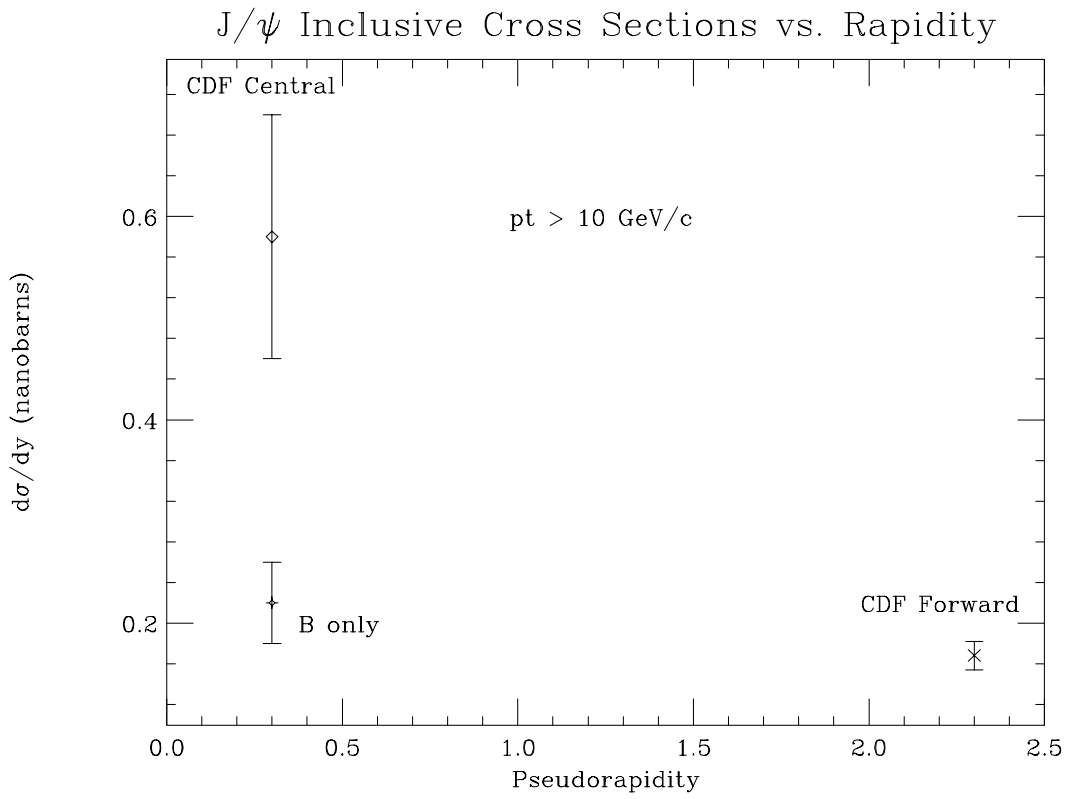

Figure 7.1: The forward muon J/ψ cross section and the CDF central result, plotted as a function of detector η.

$\psi_{p_t} > 5\ GeV/c$. In order to get the correct value, it was necessary to integrate the plot of the central differential cross section for $\psi_{p_t} > 10\ GeV/c$. The uncertainty in that integration accounts for the surprisingly large error bars shown on the point in Figure 7.1.

As stated before, the central measurement can be separated into components of prompt J/ψ production, and J/ψs which are created in B decays. So, in addition to the central inclusive cross section, the plot in Figure 7.1 also shows the measurement of the exclusive cross section from B decays (labeled "B only" in the plot).

Compare the B only central region point to the CDF forward point for the total J/ψ cross section, in Figure 7.1. It indicates that, if the B cross section stayed constant with increasing rapidity, there would be no room for direct production of J/ψs in the forward measurement.

7.2 Comparison to the D0 Forward Cross Section

In 1999, D0, the other colliding physics experiment at Fermilab, published an inclusive cross section for J/ψs that decay to forward muons [35]. Figure 7.2 shows the D0 differential cross section (squares), along with the results of this thesis (x's).

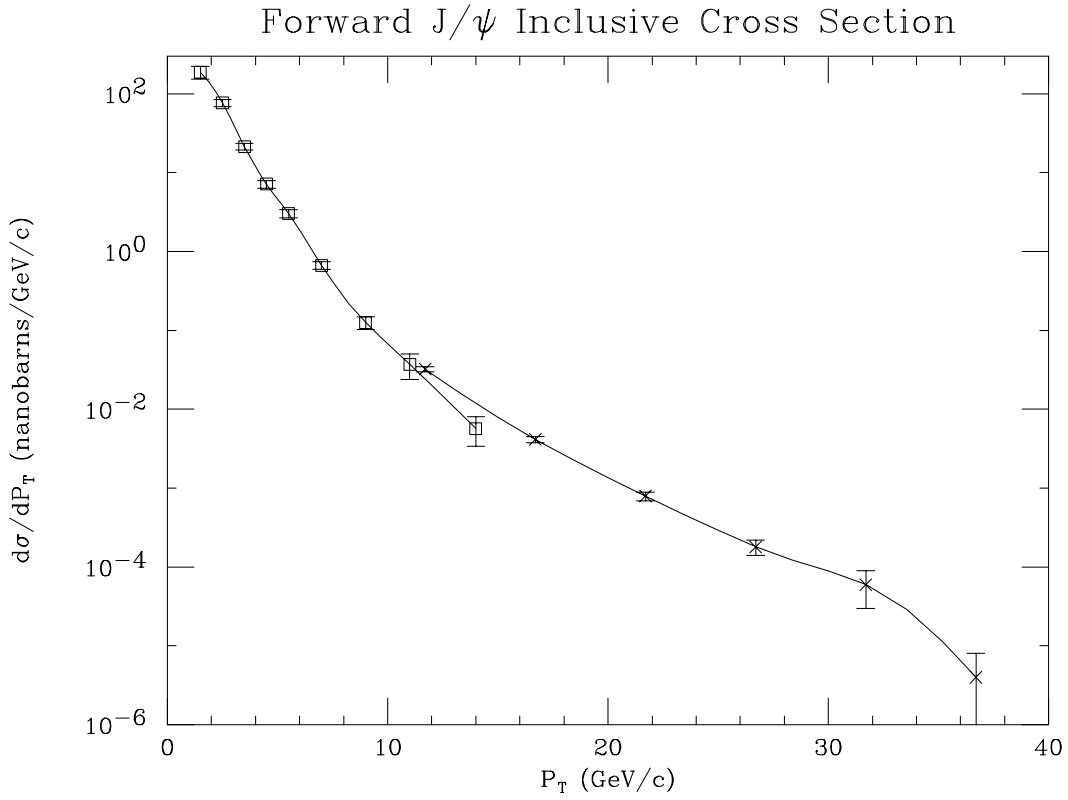

Figure 7.2: The forward muon J/ψ differential cross section, plotted as a function of p_t. The squares are results from the D0 experiment, and the X's are the results of this thesis.

An important consideration in this comparison is that the D0 measurement was carried out at a higher average pseudorapidity, $\eta = 3$. This puts the D0 result slightly farther forward, which can not be ignored when making a comparison. Therefore, for the purpose of this comparison, the D0 differential cross section measurements in Figure 7.2 should be increased by 50% , which is the amount that the total measurement presented in this thesis exceeds the total D0 measurement. This assumes that the difference in rapidity is responsible for the difference in the two measurements. These corrected data points are shown in Figure 7.3. The new D0 differential cross section points are plotted as circles, and as before, the results of this thesis are x's. The plot shows that the results of this thesis match well to the corrected D0 results, demonstrating that these results are consistent with the D0 measurement.

Figure 7.4 shows the data from Figure 7.1, along with two other CDF central data points, which are the diamonds on this plot. One is the inclusive cross section where the analysis required J/ψ transverse momentum greater than 5 GeV/c (as opposed to $p_t > 10$ GeV/c), and the other required $p_t > 8$ GeV/c. Also on this plot, are three squares showing the D0 results. The first point required J/ψ transverse momentum greater than 5 GeV/c, the second required $p_t > 8$ GeV/c, and the third required $p_t > 10$ GeV/c. The lines drawn on the plot connect measurements that have the same transverse momentum requirement.

Figure 7.4 shows that the cross section continues to decrease as one moves to higher rapidities. It also indicates that the results of the analysis presented here

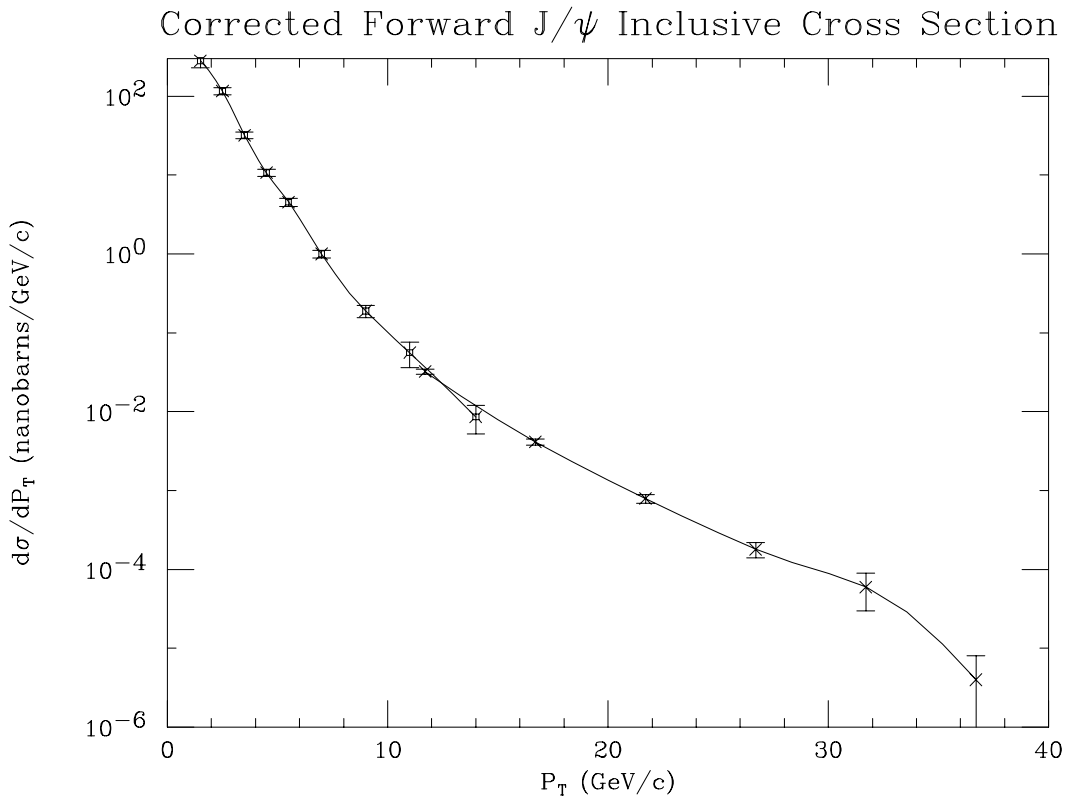

Figure 7.3: The forward muon J/ψ differential cross section, plotted as a function of p_t. The circles are results from the D0 experiment, corrected to the average rapidity of FMU, and the X's are the results of this thesis.

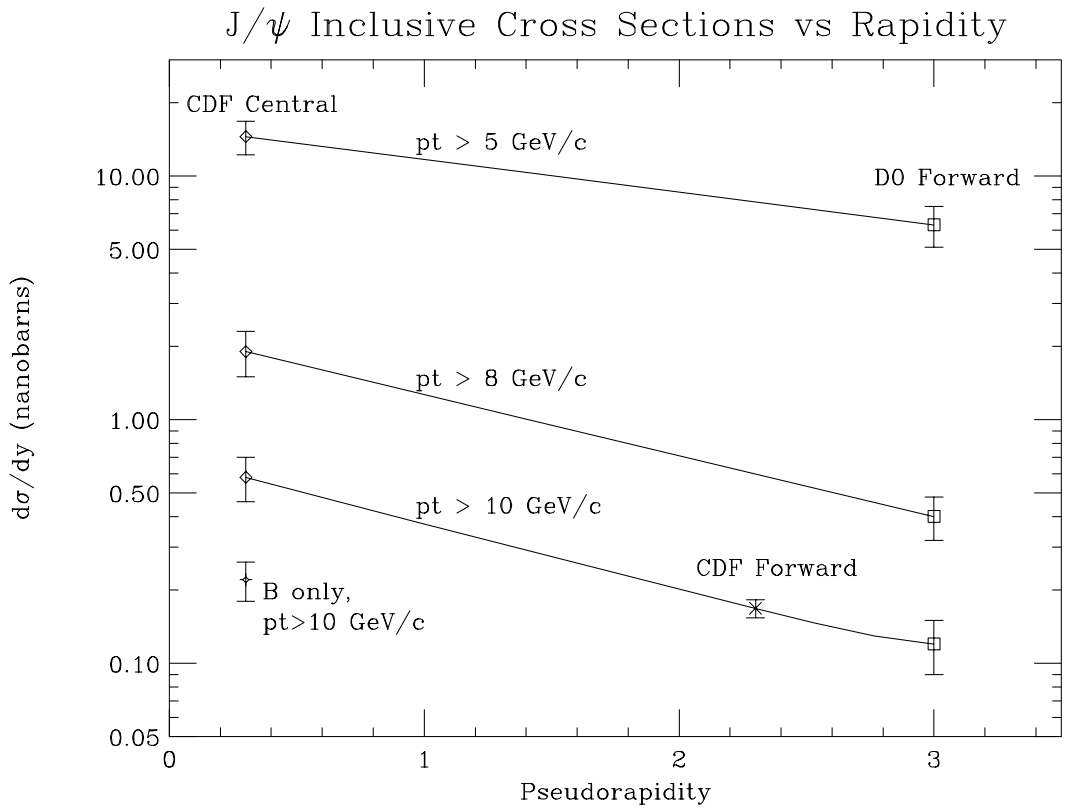

Figure 7.4: The forward muon J/ψ cross section and the CDF central result, along with the D0 forward result, plotted as a function of detector η.

are consistent with the D0 measurement.

Bibliography

[1] C. Caso *et al.* Review of Particle Physics. *Euro.Phys.J.* **C3** (1998).

[2] P. A. M. Dirac. The Quantum Theory of Electron. *Proc. Roy. Soc. Lond.* **A117**, 610–624 (1928).

[3] P. A. M. Dirac. Quantized Singularities in the Electromagnetic Field. *Proc. Roy. Soc. Lond.* **133**, 60–72 (1931).

[4] S. Glashow. Partial Symmetries of Weak Interactions. *Nucl. Phys.* **22**, 579–588 (1961).

[5] S. Weinberg. A Model of Leptons. *Phys. Rev. Lett.* **19**, 1264–1266 (1967).

[6] A. Salam. *Elementary Particle Physics.* Almquist and Wiksells Stockholm (1969).

[7] Particle Data Group. Review of Particle Properties. *Phys. Rev. D* **50**, 1173–1826 (1994).

[8] J. Iliopoulus S. Glashow and L. Maiani. Weak Interactions With Lepton-Hadron Symmetry. *Phys. Rev. D* **2**, 1285–1292 (1970).

[9] J. Aubert *et al.* Experimental Observation of a Heavy Particle J. *Phys. Rev. Lett.* **33**, 1404–1406 (1974).

[10] J. Augustin *et al.* Discovery of a Narrow Resonance in e^+e^- Annihilation. *Phys. Rev. Lett.* **33**, 1406–1408 (1974).

[11] G. Abrams *et al.* The Discovery of a Second Narrow Resonance in e^+e^- Annihilation. *Phys. Rev. Lett.* **33**, 1453–1455 (1974).

[12] R. Van Royen and V. Weisskopf. Hadron Decay Processes and the Quark Model. *Nuovo Cim* **50**, 617–645 (1967).

[13] R. Van Royen and V. Weisskopf. Hadron Decay Processes and the Quark Model. *Nuovo Cim* **51**, 583 (1967).

[14] F. Abe *et al.* J/ψ and $\psi(2S)$ Production in $\bar{p}p$ Collisions at $\sqrt{s} = 1.8$ TeV. *Phys. Rev. Lett.* **79**, 572–577 (1997).

[15] P. Cho and A. K. Leibovich. Color-Octet Quarkonia Production. *Phys. Rev. D* **53**, 150–162 (1996).

[16] P. Cho and A. K. Leibovich. Color-Octet Quarkonia Production II. *Phys. Rev. D* **53**, 6203–6217 (1996).

[17] S. Fleming. Onium Production. In *Workshop on Heavy Quark Physics at C-Zero* volume 2. Fermi National Accelerator Laboratory, unpublished (1996).

[18] S. Frixione *et al.* Heavy-Quark Production. In Buras and Lindner, editors, *Heavy Flavors II* volume 15 of *Advanced Series on Directions in High Energy Physics* pages 609–706. World Scientific (1998).

[19] D. Zieminska. Inclusive b Quark Production at CDF and D0. *International Conference on High Energy Physics* **1**, 922–925 (1996).

[20] F. Abe *et al.* The CDF Detector: An Overview. *Nucl. Instr. and Meth. A* **271**, 387–403 (1988).

[21] J. Skarha. *Forward Muon Production in Proton-Antiproton Collisions at* $\sqrt{s} = 1.8$ *TeV.* PhD thesis University of Wisconsin (1989).

[22] L. Markosky. *A Measurement of the Forward-Backward Asymmetry and* $sin^2\theta_W$ *from the Process* $Z^0 \rightarrow \mu^+\mu^-$ *at* $\sqrt{s} = 1.8$ *TeV.* PhD thesis University of Wisconsin (1992).

[23] J. Lamoureux. *Direct* $\bar{b}b$ *Production in* $\bar{p}p$ *Collisions at* $\sqrt{s} = 1.8$ *TeV.* PhD thesis University of Wisconsin (1993).

[24] K. Byrum *et al.* Forward Muon Chamber Efficiency, Gain and Resolution Studies. CDFNOTE 1343 (1991).

[25] D. Carlsmith and J. Skarha. Forward Muon Tracking Code. CDFNOTE 925 (1989).

[26] K. Byrum. *The Lepton Charge Asymmetry from $W \to \mu\nu$ Using Forward Muons at CDF.* PhD thesis University of Wisconsin (1992).

[27] J. Olsen. Correlated Forward-Central $\bar{b}b$ Production. CDFNOTE 4105 (1997).

[28] J. Bellinger *et al.* $W \to \mu\nu$ Charge-Asymmetry with Forward Muons. CDFNOTE 3410 (1995).

[29] D. Cronin-Hennessy and A. Beretvas. Luminosity at CDF. CDFNOTE 4721 (1998).

[30] F. Abe *et al.* Measurement of the B Meson Differential Cross Section $d\sigma/dp_t$ in $\bar{p}p$ Collisions at $\sqrt{s} = 1.8$ TeV. *Phys. Rev. Lett.* **75**, 1451–1455 (1995).

[31] R. Balest *et al.* Inclusive Decays of B Mesons to Charmonium. *Phys. Rev.* **D52**, 2661–2672 (1995).

[32] S. D. Drell and Tung-Mow Yan. Massive Lepton Pair Production in Hadron-Hadron Collisions at High-Energies. *Phys. Rev. Lett.* **25**, 316–320 (1970).

[33] Vernon D. Barger and Roger J. N. Phillips. *Collider Physics.* Addison-Wesley Menlo Park (1987).

[34] D. W. Duke and R. G. Roberts. Determinations of the QCD Strong Coupling α_s and the Scale Λ_{QCD}. *Phys. Rep.* **120**, 275–365 (1985).

[35] B. Abbott *et al.* Small Angle J/ψ Production in $\bar{p}p$ Collisions at $\sqrt{s} = 1.8$ TeV. *Phys. Rev. Lett.* **82**, 35–40 (1999).